



HAL
open science

Reassessment of the rifting process in the Western Corinth Rift from relocated seismicity

Sophie Lambotte, Hélène Lyon-Caen, Geneviève Patau, Alexandre Nercessian, Francesco Pacchiani, Seid Bourouis, M Drilleau, P Adamova, Anne Deschamps, Pascal Bernard

► To cite this version:

Sophie Lambotte, Hélène Lyon-Caen, Geneviève Patau, Alexandre Nercessian, Francesco Pacchiani, et al.. Reassessment of the rifting process in the Western Corinth Rift from relocated seismicity. *Geophysical Journal International*, 2014, 197 (3), pp.1822-1844. 10.1093/gji/ggu096 . hal-01531793

HAL Id: hal-01531793

<https://hal.science/hal-01531793>

Submitted on 1 Jun 2017

HAL is a multi-disciplinary open access archive for the deposit and dissemination of scientific research documents, whether they are published or not. The documents may come from teaching and research institutions in France or abroad, or from public or private research centers.

L'archive ouverte pluridisciplinaire **HAL**, est destinée au dépôt et à la diffusion de documents scientifiques de niveau recherche, publiés ou non, émanant des établissements d'enseignement et de recherche français ou étrangers, des laboratoires publics ou privés.

Reassessment of the rifting process in the Western Corinth Rift from relocated seismicity

S. Lambotte,^{1,2} H. Lyon-Caen,¹ P. Bernard,³ A. Deschamps,⁴ G. Patau,³ A. Nercessian,³ F. Pacchiani,^{1,*} S. Bourouis,⁵ M. Drilleau^{1,†} and P. Adamova^{1,‡}

¹Laboratoire de Géologie, Ecole Normale Supérieure, CNRS, Paris, France. E-mail: sophie.lambotte@unistra.fr

²Institut de Physique du Globe de Strasbourg, CNRS UMR7516, Strasbourg, France

³Département de sismologie, Institut de Physique du Globe de Paris, CNRS, Paris, France

⁴Géoazur, Université de Nice Sophia Antipolis, CNRS, Valbonne – Sophia Antipolis, France

⁵Centre de Recherche en Astronomie, Astrophysique et Géophysique, Route de l'observatoire, 16006 Bouzareah, Algeria

Accepted 2014 March 12. Received 2014 March 11; in original form 2013 March 7

SUMMARY

The seismic activity in the western part of the Corinth Rift (Greece) over the period 2000–2007, monitored by a dense network of three-component stations, is analysed in terms of multiplets and high precision relocation using double difference techniques. This detailed analysis provides new insights into the geometry of faults at depth, the nature and the structure of the active zone at 6–8 km depth previously interpreted as a possible detachment, and more generally into the rifting process. The seismicity exhibits a complex structure, strongly varying along the rift axis. The detailed picture of the seismic zone below the rift indicates that its shallower part (at depths of 6–8 km) is 1–1.5 km thick with a complex microstructure, and that its deeper part (at depths of 9–12 km) gently dipping to the north (10–20°) is 0.1–0.3 km thick with a microstructure consistent with the general slope of the structure. Although the nature of this seismic zone remains an open question, the presence of seismicity beneath the main active area, the strong variability of the structure along the rift over short distances and the complex microstructure of the shallower part revealed by the multiplet analysis are arguments against the hypothesis of a mature detachment under the rift: this active zone more likely represents a layer of diffuse deformation. The geometry of the mapped active faults is not well defined at depth, as no seismicity is observed between 0 and 4 km, except for the Aigion Fault rooting in the seismic layer at 6 km depth with a dip of 60°. A distinct cloud of seismicity may be associated with the antithetic Kalithea Fault, on which the 1909 Fokis earthquake ($M_s = 6.3$) may have occurred. The link between the 1995 rupture ($M_s = 6.2$) and the faults known at the surface has been better constrained, as the relocated seismicity favours a rupture on an offshore, blind fault dipping at 30°, rather than on the deeper part of the East Helike Fault. Consequently, the 1995 event is expected to have decreased the Coulomb stress on the East Helike Fault. To explain these seismic observations along with the geodetic observations, a new mechanical model for the rifting process in this region is proposed, involving non-elastic, mostly aseismic uniform NS opening below the rift axis, coupled with the downward and northward growth of a yet immature detachment: the reported GPS rates would mainly result from this deep, silent source, and the seismicity would reveal the detachment position, not yet connected to the ductile lower crust. In such a model, the strong fluctuations of microseismicity would result from small strain instabilities, undetected by continuous GPS and possibly related to pore pressure transients.

Key words: Seismicity and tectonics; Continental tectonics: extensional; Dynamics and mechanics of faulting.

*Now at: Addax Petroleum, Geneva, Switzerland.

†Now at: Laboratoire de Planétologie et Géodynamique, CNRS, Nantes, France

‡Now at: Academy of Sciences, Institute of Geophysics, Prague, Czech Republic.

1 INTRODUCTION

For more than two decades, the Corinth Rift in Central Greece has been the target of a large number of geological (e.g. Ori 1989; Doutsos & Poulimenos 1992; Armijo *et al.* 1996; Sachpazi *et al.* 2003; Ghisetti & Vezzani 2005; Rohais *et al.* 2007), geodetic (Billiris *et al.* 1991; Clarke *et al.* 1997; Briole *et al.* 2000; Avallone *et al.* 2004, for example) and seismic studies (e.g. Jackson *et al.* 1982; Rigo *et al.* 1996; Latorre *et al.* 2004; Gautier *et al.* 2006; Pacchiani & Lyon-Caen 2010), however the fault geometry at depth and the rifting process are still debated. Is rifting asymmetric or symmetric? Is there a detachment at 6–8 km depth? In the western part of the rift, seismicity studies highlight the existence of a 3- to 4-km-thick active layer below the rift, dipping to the north at a low-angle ($\sim 10\text{--}20^\circ$; Rigo *et al.* 1996; Lyon-Caen *et al.* 2004; Bernard *et al.* 2006; Gautier *et al.* 2006; Bourouis & Cornet 2009), and including small earthquakes with geometries and focal mechanisms indicating slip on low-angle fault planes ($\sim 10\text{--}20^\circ$; Rietbrock *et al.* 1996; Rigo *et al.* 1996; Pacchiani 2006). Three main hypotheses have been proposed to explain the existence and the deformation mechanism of this seismically active zone: (1) a low-angle normal fault or shallowly north dipping detachment zone onto which major normal faults are rooting and which acts as a shear zone (Rigo *et al.* 1996; Bernard *et al.* 2006), (2) block deformation (Cianetti *et al.* 2008) and (3) brittle-ductile transition (Hatzfeld *et al.* 2000).

The mechanical conditions under which seismic slip on low-angle normal faults ($\leq 30^\circ$) may occur is still debated (e.g. Rice 1992; Wernicke 1995; Abers 2009; Colletini 2011; Lecomte *et al.* 2012) but fluids probably play a significant role (Rice 1992; Lecomte *et al.* 2012). Although low-angle normal faults in extensional regions are clearly observed in the field and in seismic reflection profiles [e.g. Santa Rita Fault of the Tucson Basin (Johnson & Loy 1992); the Lamaille Valley Fault in the Basin and Range (Smith *et al.* 1989; Wernicke 1995)], only a few seismically active low-angle normal faults are documented apart from the Corinth Rift, the Woodlark–D’Entrecasteaux Rift zone, Papua New Guinea (e.g. Abers *et al.* 1997; Taylor *et al.* 1999), Altotiberina Fault, Umbria region, Italy (e.g. Boncio *et al.* 2000; Chiaraluze *et al.* 2007; Brozzetti *et al.* 2009), Colfiorito Fault, Italy (e.g. Boncio *et al.* 2000) and Tibet (Monigle *et al.* 2012). Because of its high strain and seismicity rates, the western Corinth Rift is a good target to better understand low-angle normal faulting.

Using relocated seismicity, the aim of this paper is to present new insights into the relationships between deep structures and faults observed at the surface or imaged by seismic/bathymetric studies, the nature and structure of the shallowly dipping seismic layer below the rift and more generally into the rifting process. Considering the seismicity recorded by the CRLNET local network (Lyon-Caen *et al.* 2004, <http://crlab.eu>) between 2000 and 2007 in the western part of the rift, we performed a detailed relocation using a double difference technique (Waldhauser & Ellsworth 2000), and combined it with a multiplet analysis to improve the precision of relocated seismicity and to identify microstructures within the seismicity. After a brief description of the data set, we explain the method used to identify multiplets and to relocate the seismicity. We then present the high-resolution relocation results, describing in detail fault geometries at depth, and the possible association with past earthquakes, and more briefly the spatio-temporal evolution of the microseismicity. We finally discuss the seismic structures and some mechanical models to explain the observed seismicity.

2 TECTONIC SETTING

The Corinth Rift in Central Greece is one of the most active area in Europe with several instrumental and historical earthquakes of magnitude larger than 5.5 (Jackson *et al.* 1982; Ambraseys & Jackson 1990; Papazachos & Papazachou 1997; Hatzfeld *et al.* 2000; Makropoulos *et al.* 2012), numerous swarms [1991: Rigo *et al.* (1996), 2001: Pacchiani & Lyon-Caen (2010), 2002: Bernard *et al.* (2010), 2009: Barnoud (2012), 2010–2011: Sokos *et al.* (2012)] and a significant background seismicity (Fig. 1). It appears as an E–W striking asymmetric rift, with the main active faults cropping out on the southern coast of the gulf, dipping to the north at $40\text{--}60^\circ$. This results in a long-term subsidence of the northern coast and an uplift of the southern coast, superimposed to the general uplift of the northern Peloponnese (Armijo *et al.* 1996). Some active offshore and onland antithetic faults have also been identified (Stefatos *et al.* 2002; Moretti *et al.* 2003; Gallousi & Koukouvelas 2007; Bell *et al.* 2008; Balkaniotis 2009; Taylor *et al.* 2011). The Corinth Rift cuts obliquely across the NNW–SSE Hellenides mountain belt, made of a succession of carbonate-flysch nappes. Some inherited complex structures of this pre-rift thrust belt seem to have influenced sedimentation and fault segmentation (Ghisetti & Vezzani 2004, 2005), and may explain the lateral variability of structures along the rift from east to west. The extension has a mean $N5^\circ$ direction and its rate across the rift increases from 11 mm yr^{-1} to the east to 16 mm yr^{-1} to the west (Billiris *et al.* 1991; Briole *et al.* 2000; Avallone *et al.* 2004). In the western part of the rift, GPS studies have shown that the deformation gradient is localized offshore on a 10-km-wide zone (Briole *et al.* 2000; Avallone *et al.* 2004). This implies a very high strain rate, associated with the observed high seismicity rate (Lyon-Caen *et al.* 2004; Bourouis & Cornet 2009). The northern and southern blocks act as rigid tectonic units, except in some localized areas like the vicinity of the Pspathopyrgos Fault (PsF) at the western end of the rift.

During the rift history, starting around 5 Ma, a northward migration of fault activity occurred (Goldsworthy & Jackson 2001; Ford *et al.* 2012), resulting in the current localization of the main active faults along the southern coastline. Therefore, the recent morphological architecture in the western part of the rift is mainly controlled by the north dipping faults along the coast (Fig. 1)—from west to east: Pspathopyrgos Fault (PsF), Kamarai-Lambiri Fault system [KLF; also named Neos-Erimeos Fault system, including the Lambiri Fault, the Selianitika Fault and the Fassouleika Fault (e.g. Pantosti *et al.* 2004; Palyvos *et al.* 2005)], Aigion Fault (AiF) and East Helike Fault (EHF). Some offshore and onland south dipping faults may also play a role, but have been less extensively studied than the north dipping ones—from west to east: Marathia Fault (MrF), Mornos Fault (MnF), Trizonia Fault (TrF), West and East Channel faults (WCF, ECF) and South Eratini faults (SEF; Bell *et al.* 2008, 2009). The faults located more to the south—from west to east: Lakka Fault (LakF), West Helike Fault (WHF), Pirgaki Fault (PiF) and Mammaoussia Fault (MmF)—are thought to be less active or completely deactivated (e.g. Flotté 2003; Pantosti *et al.* 2004; Ford *et al.* 2012).

Several large historical events have been reported with estimated magnitude around 6 or larger, hitting either the northern or the southern coast (Fig. 1, orange/red boxes), but few of these events have been unambiguously associated with one of the main faults: the 1861 earthquake (Schmidt 1881; Mouyaris *et al.* 1992) is known to be related to the EHF as surface breaks were observed, and the same is likely for the 373 BC event (Mouyaris *et al.* 1992; Stewart 1996; Soter & Katsonopoulou 1999). With less certainty, the 1817

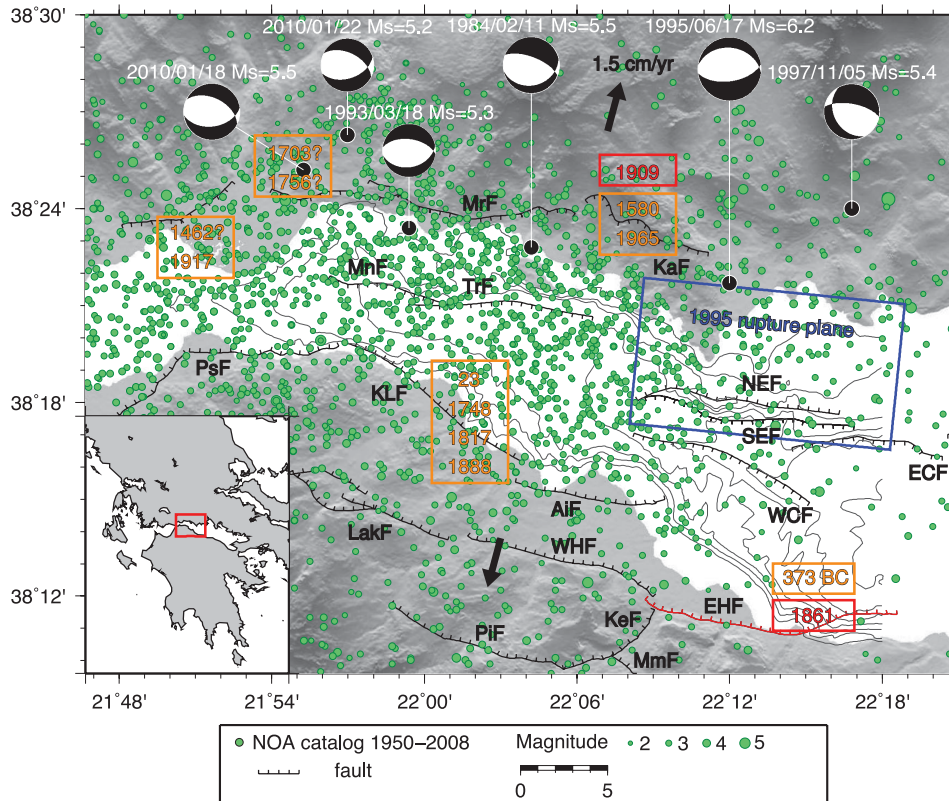


Figure 1. Seismicity of the studied area from 1950 to 2008. Data are from the National Observatory of Athens' catalogue (locations are rounded to the minute) randomized with random shift between $0'$ and $1'$ for visual account of density. Focal mechanisms are from Bernard *et al.* (1997); Sokos *et al.* (2012) and the global CMT catalogue. Historical earthquakes are indicated in orange and red (from Ambraseys & Jackson 1990; Papazachos & Papazachou 1997), red events are discussed in this paper. Black arrows indicate the geodetic rift opening direction (Briole *et al.* 2000; Avallone *et al.* 2004). Faults traces have been compiled by N. Meyer (PhD thesis in preparation) based on Moretti *et al.* (2003), Palyvos *et al.* (2005), Bell *et al.* (2008) and new field work. Main fault names are indicated: PsF, Psathopyrgos Fault; LakF, Lakka Fault; MmF, Mamoussia Fault; PiF, Pirgaki Fault; WHF, West Helike Fault; TrF, Trizonia Fault; MnF, Mornos Fault; EHF, East Helike Fault; AiF, Aigion Fault; KeF, Kerinitis Fault; KLF, Kamarai and Lambiri Fault system; WCF, West Channel Fault; ECF, East Channel Fault; SEF, South Eratini Fault; KaF, Kalithea Fault; MrF, Marathia Fault; NEF, North Eratini Fault. The projection to the surface of the 1995 rupture plane is indicated by a blue rectangle.

and 1888 events hit the city of Aigion and may be associated to the AiF (Papazachos & Papazachou 1997; Pantosti *et al.* 2004).

Even for recent events, linking a rupture to a fault remains difficult as the fault geometry at depth is not well constrained; indeed a major earthquake ($M_s = 6.2$) occurred in 1995 on a low-angle north dipping fault plane ($\sim 30^\circ$; Bernard *et al.* 1997), linking its rupture to faults at the surface is still a matter of debate (e.g. Bell *et al.* 2008; Taylor *et al.* 2011) although this has critical implications in terms of seismic hazard. The 1992 Galaxidi ($M_s = 5.8$) earthquake (Hatzfeld *et al.* 1996) located a few kilometres further east probably occurred on a similar shallow north dipping nodal plane.

3 DATA ANALYSIS

To obtain a high-resolution picture of the seismicity at depth, we proceed in two steps: (1) identification of multiplets and (2) relocation of the whole seismicity using a double difference technique. We here describe the data set used and the two steps of the process.

3.1 Network and data

The Corinth Rift Laboratory network (CRLNET) has been installed since 2000 in the western part of the rift around the city of Aigion, and covers a 30×30 km area (Lyon-Caen *et al.* 2004; Bernard

et al. 2006, see Fig. 2). This network is composed of 12 stations recording at 125 Hz equipped with short-period three-component seismometers: seven on the southern coast installed in 80- to 120-m-deep boreholes and five on the northern coast. In addition, we also use data from four stations recording at 100 Hz equipped with broad-band seismometers: SERG (operated by Charles university in Prague in collaboration with Patras university), LAKA and DAFN (operated by Athens university) and SEL (operated by Patras university). More than 10 yr of seismicity is now available. In this paper, we present the results of 7 yr of data analysis from spring 2000 to spring 2007 (about 49 800 events). Data from two temporary experiments are also integrated: a 9-d post-seismic deployment in 1995 after the Aigion earthquake (Bernard *et al.* 1997) with 20 stations equipped with 10 vertical and 10 three-component seismometers and recording at 50 or 200 Hz depending on the stations, and a 6-week experiment in 1991 (Rigo *et al.* 1996) covering an area of 40×40 km with 51 stations equipped with 21 vertical and 30 three-component seismometers and recording at 62.5, 100, 125 or 200 Hz depending on the stations.

All data from the 1991 and 1995 experiments have been picked manually. Events from the continuous CRLNET stations are extracted using a post-trigger algorithm that detects an event when more than three stations trigger at about the same time (within 2 s) based on a STA/LTA (short-term average/long-term average)

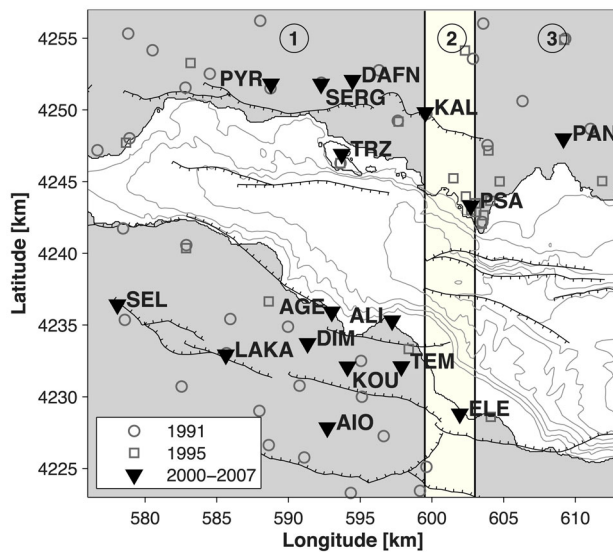


Figure 2. Map of the seismic stations used in this analysis. Stations from the 1991 experiment are indicated by grey circles, the ones from the 1995 experiment by grey squares and the stations used during the 2000–2007 period are indicated by black reverse triangles (it includes stations from the CRL network, some broad-band stations operated by Athens University, Patras University and Charles University, Prague). The three zones numbered from 1 to 3 have different seismicity structures and rates, and are referred in the text as: (1) Western Zone (ZW), (2) Transition Zone (ZT) and (3) Eastern Zone (ZE). Main faults as in Fig. 1.

ratio. All these events are automatically located using P and S picks. Preliminary location is done using hypo71 software (Lee & Lahr 1972), the 1-D velocity model of Rigo *et al.* (1996) and a V_P/V_S ratio of 1.80. Depending on the number of phases picked, the average standard errors range from 500 m to a few kilometres for events in the networks, and reach 5–6 km for events outside the networks. More details on the detection and picking algorithms can be found in Bourouis & Cornet (2009). Part of the data set (35 per cent) has been manually picked for specific studies. If available, manual picks are used instead of automatic ones. A statistical analysis of the time differences between automatic and manual picks for events having both manual and automatic picks has shown differences generally lower than 0.14 s for P waves (95 per cent confidence interval), and lower than 0.54 s for S waves (95 per cent confidence interval) depending on the quality of stations and phase onsets. The distribution of these time differences for P wave is quite symmetric. For the S waves, however the distribution is not symmetric, the automatic picks being often late with respect to the manual ones. The average time reading precision is estimated to be 0.03 s and 0.06 s for manual P and S pickings and to be 0.07 s and 0.29 s for automatic P and S pickings. Differences in horizontal location between manual and automatic picking are less than 2 km and differences in depth are less than 3 km for most of the events. Moment magnitudes estimated from spectral amplitude fit range from 0.5 to 4.5. The catalogue is complete down to $M_w = 1.4$ (Pacchiani 2006; Wyss *et al.* 2008).

3.2 Multiplet classification

A multiplet is a set of earthquakes having similar waveforms and focal mechanisms, close in location, often associated to small asperities (e.g. Geller & Mueller 1980; Tsujiura 1983; Deich-

mann & Garcia-Fernandez 1992; Vidale *et al.* 1994; Nadeau & Johnson 1998). Cross-correlation analyses are used to identify multiplets, the resulting cross-correlation time-shifts are commonly used to perform high-precision relocations at local or regional scale (e.g. Frémont & Malone 1987; Got *et al.* 1994; Rubin *et al.* 1999; Battaglia *et al.* 2004; Hauksson & Shearer 2005; Waldhauser & Schaff 2008; Kapetanidis & Papadimitriou 2011), or to study medium velocity variations (e.g. Poupinet *et al.* 1984; Cociani *et al.* 2010). In addition, the detailed geometry of the multiplets provides additional information on the microstructure of the seismicity, useful for characterizing seismically active structures (e.g. Rietbrock *et al.* 1996; Moriya *et al.* 2003; Carmona *et al.* 2010; Pacchiani & Lyon-Caen 2010). To classify events in multiplets, waveform similarity of P phases is evaluated using cross-correlations between events. In order to reduce computation time, we do not cross-correlate all events with each other. We scan the database event by event; the second event is cross-correlated with the first one, the third event with the first two events and so on; either the event is classified as a multiplet with one of the earlier ones, or it becomes an independent event. When a multiplet is identified, the event having the maximum number of station readings is chosen as the reference event. Then all the events of a multiplet are represented by the reference event in the cross-correlation procedure, reducing the number of cross-correlations to compute. This procedure is used only for classification, not for the relocation process. Cross-correlations are computed in the time domain for time windows containing P waves, first at the time resolution of one sample, and finally at subsample time resolution using a local polynomial fit. This procedure enables the measurement of delays within millisecond precision, and allows better estimations for large delays (Schaff *et al.* 2004). Data are filtered between 3 and 20 Hz. The length of the time window used is 1 s in order to exclude S waves. Because of larger errors on automatic picks, three time-shifted windows are used to ensure that the P wave is included: the first window is defined using the P pick (beginning of the window at 0.1 s before P pick), and the two other windows are shifted, respectively, towards positive and negative time. The best cross-correlation measurement of the three windows is kept. As already mentioned, the time differences between automatic and manual picks are smaller than 0.2 s for most of the P waves. Therefore, we choose 0.3 s for the maximum window time-shift for P waves in order to be able to include the P -wave energy. The condition to add an event to an existing multiplet is a minimum of 5 P waves with a cross-correlation coefficient greater than 0.80. For events recorded by less than five stations, the condition is relaxed and depends on the number of stations that have recorded the event. The criteria for multiplet classification are quite strong, but they have been chosen to obtain an accurate image of individual multiplet geometry and to allow microstructure studies. Weaker criteria would result in the classification of more events but with less similarities. Fig. 3 presents a multiplet recorded at several stations.

Both manually and automatically picked events are combined. Multiplets are independently searched for in the CRLNET database and in the two temporary experiment databases, as no stations are common to the three experiments. Over half of the data set (~55 per cent) can be classified in multiplets, among those 48 per cent are doublets. Some of these multiplets are clustered in time, other last several years (Fig. 3).

3.3 Seismicity relocation

Once the multiplet classification was done, we performed the relocation using the double-difference algorithm hypoDD (Waldhauser &

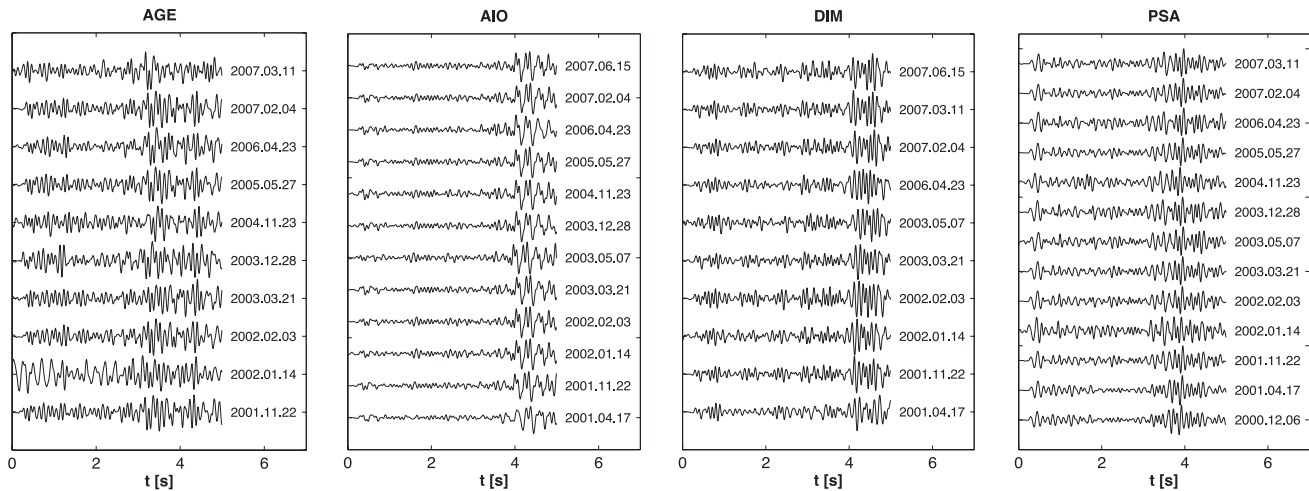


Figure 3. Example of a multiplet recorded at four stations. Each panel corresponds to the waveforms of the vertical component of each station, and each line to an event. The date of the event occurrence is indicated to the right of each waveform. This multiplet is located near Pyrgos station (PYR), and includes events from 2002 to 2007. Data are filtered between 3 and 20 Hz. The correlation of all events together gives cross-correlation coefficients from 0.85 to 0.96.

Ellsworth 2000, for example). The inverse problem is solved using a damped least-square technique, minimizing the residuals between observed and calculated phase delay times between a pair of adjacent earthquakes recorded at common stations; this reduces the bias due to model errors along the path. The 1-D velocity model used is the same as the one used for absolute locations (Rigo *et al.* 1996, with a V_p/V_s ratio of 1.80). Differential times are based on catalogue picks and are combined with cross-correlation measurements. Delays from cross-correlation are used both for P and S waves. The cross-correlation computation is quite similar to the one used for the multiplet classification. We used the same filtering, and the computation is made in the time domain. However, we considered two window lengths, of 1 and 1.5 s, and check the consistency of measurements obtained for the two window lengths to reduce the number of outliers due to cycle skipping (Schaff *et al.* 2004). The time-shifts from the 1-s window length were kept in the relocation process. The cross-correlations were computed for all events in multiplets as well as for events of neighbouring multiplets and isolated events in a radius of about 5 km.

The data were *a priori* weighted using different schemes. Cross-correlated data were weighted by their squared cross-correlation coefficient without any difference between P and S waves. Catalogue data were weighted using two qualities: (1) the pick quality and (2) the quality of the location. The pick quality was assigned by the operator having manually reviewed the event or assigned by default for automatic events. It is indicated by a number between 0 and 3. The automatic picked data were downweighted relative to the manually picked ones by decreasing their pick quality by 2 points, in order to take into account the difference in accuracy. By default, the qualities assigned to automatic picks are 0 for P wave and 1 for S wave; then, they were decreased, respectively, to 2 and 3. The automatic picked data were also downweighted using the noise level at the stations. The quality location given as output of hypo71 is indicated by a letter between ‘A’ and ‘D’ and is based on the rms, the horizontal and vertical errors, the number of phases used for the location, the azimuthal gap and the distance to the closest station. We, respectively, assigned to this quality a number between 0 and 3, and computed a combined quality for each phase by multiplying the two qualities. A weighting between 1 and 0 is then, respectively, assigned to the obtained quality (from 0 to 9).

This weighting scheme allows in particular to reduce the impact of events having large azimuthal gaps and therefore having location closer to the network than their true location.

For the relocation, we excluded events having no location (~ 5 per cent) and events located too far from the network (≥ 10 km) as their locations are not well enough constrained (~ 27 per cent). For the automatically located events, we only kept well-located events having at least five P and three S phases and located with errors lower than 5 km (~ 50 per cent, the standard average errors are of the order of 1–3 km for events being in the networks), and events being in multiplets. After relocation, only 13 000 events (~ 26 per cent of the total number of events) were kept. Small magnitude events, as well as isolated events, were often removed, as they are weakly linked to their neighbours.

To assess the relative relocation errors, we applied a statistical resampling method using the bootstrap technique (Efron 1982; Efron & Tibshirani 1993). We evaluated the influence of: (1) an event on the location of all others, (2) the station coverage and (3) the uncertainties of the traveltime differences. Considering the influence of an event on the location of the other, relative location errors are typically a few metres, except for a few events having relative errors that range from a few tens of metres to a few hundreds of metres. Considering the influence of the station coverage, relative location errors range from a few metres to a few tens of metres for events located a few kilometres outside the network; the larger errors are observed to the west, where the network coverage is poor. Finally, considering the uncertainties of the traveltime differences, relative location errors range from a few metres for adjacent events mainly constrained by cross-correlation data to a few hundred of metres for events a few kilometres apart constrained by absolute time catalogue differences. In conclusion, the relative locations are well constrained in the centre of the rift where there is a high density of events with a lot of multiplets where maximal errors are of the order of 30 m, and less well constrained to the west where maximal errors are of the order of 200–300 m (Fig. B1). Errors in latitude, longitude and depth have a similar order of magnitude. Thus, the high resolution of the performed relocation enables the observed seismicity structures to be analysed in detail. Figs C1 and 9 present the seismicity before and after relocation, showing the improvement due to the relocation process.

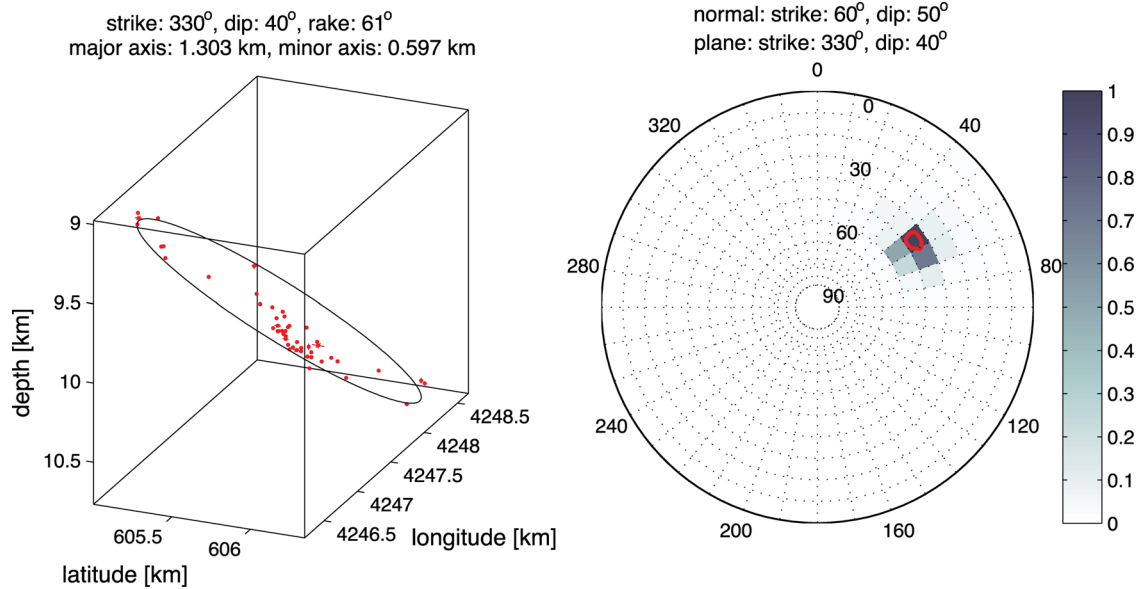


Figure 4. Example of multiplier geometry analysis. The multiplier is located to the northeastern limit of the studied area (id 2423). (a) adjustment of an ellipse to the multiplier: determination of the plane including the ellipse by performing a grid search minimizing the event distances to the plane, and determination of the best ellipse in the plane coordinates. Each red point corresponds to an event of the multiplier. The adjustment is done after relocation. (b) Lower hemisphere stereographic projection representing the pole density distribution of the normal to the plane through the set of events of the multiplier. The pole density is normalized. Red line indicates a probability larger than 0.80. The characteristics of the plane that contains the multiplier are obtained by the three points method. Dip and azimuth of the normal to the plane are respectively indicated along the radius and the circumference of the diagram.

3.4 Multiplier analysis

Considering a multiplier as a fault patch, we determined the multiplier geometry after relocation by adjusting an ellipse to the multiplier (Fig. 4). For this purpose, we first fitted a plane to the set of events of the multiplier, by performing a grid search minimizing the distance of events to the plane. This process is more robust than a least-squared fit, as it is less sensitive to the presence of outliers. Then, we computed the projection of each event to the plane, and finally estimated the characteristics (centre, length of the major and minor axes and azimuth of the major axis) of the best ellipse in the plane coordinates. The quality of the fit was evaluated using the event distances to the plane that includes the ellipse. The errors were computed taking into account the errors on the event locations. We performed a Monte Carlo simulation: at each simulation the event locations are perturbed with random uniform deviates between \pm their relocation errors. The estimated errors are larger for multipliers having small dimensions as orientation of the plane is more sensitive to event location errors. The ellipse adjustment has been done for all the multipliers with more than 20 events. All the events in these multipliers have been picked manually to increase the resolution of the relocation, and be able to discuss the results in terms of microstructure. This adjustment is not successful for all the multipliers as some are clearly non-planar. Results for planar multipliers are presented in Table A1 and Figs 5, 7, 8 and 9. To check the geometries inferred from the ellipses, results were compared with a statistical method called the three point method (Fehler *et al.* 1987). It consists of computing the poles to the planes associated with each combination of three hypocentres. The pole density is then represented using a stereographic projection; the maximum of the pole density distribution defines the geometry of the multiplier. Results obtained by the two methods are consistent within a mean difference of 10–20° for strikes and 5–10° for dips (Fig. 4). The first method has the advantage of also estimating the dimensions of the patch (major/minor axes and rake of the ellipse).

Generally, the multiplier geometries are consistent with the fault plane solutions from previous studies (Rietbrock *et al.* 1996; Rigo *et al.* 1996; Pacchiani 2006). However, a detailed comparison of the obtained multiplier geometries with focal mechanisms is beyond the scope of this paper. Godano *et al.* (2012) determine the fault plane solutions for the largest multipliers identified in this study. The results, very consistent with the geometries obtained in this study, are discussed in a companion paper (Godano *et al.*, submitted to *GGU*).

4 SEISMICITY STRUCTURES

After the relocation process, we obtained a high-precision picture of the seismicity at depth. Figs 5, 7, 8 and 9 present: (1) the relocation results and (2) the geometry of the largest multipliers. Fig. 6 indicates the main structures described in this section. It can be first noted that the 7 yr of seismicity recorded by the CRLNET network between 2000 and 2007 does not represent an overall picture of the seismicity. Indeed, the 1991 swarm (Rigo *et al.* 1996) located beneath the southern coast (green dots in Fig. 8, section a_4) and some aftershocks of the 1995 earthquake (red dots in Fig. 8, sections a_2 – a_4) are located in areas with nearly no seismicity during the studied period. Recently, a swarm in 2009 located close to the PsF also occurred in an area with low background seismic activity (see the seismicity archive map in www.crlab.eu).

A difference in the seismicity pattern is clearly observed between the eastern and the western side of the studied area, delineated by a linear NS boundary (Fig. 8: section a_2 , ivory coloured strip in Fig. 5, and grey strip in Fig. 7, sections b_1 and b_2). For this discussion, we have divided the area in three sectors (Fig. 2): (1) western zone (ZW), (2) transition zone (ZT) and (3) eastern zone (ZE). In the ZW, the seismicity rate is high with about 10 events per days (up to 150 events per day during seismic crises), and the seismicity structure is complex with a strong lateral variability over short

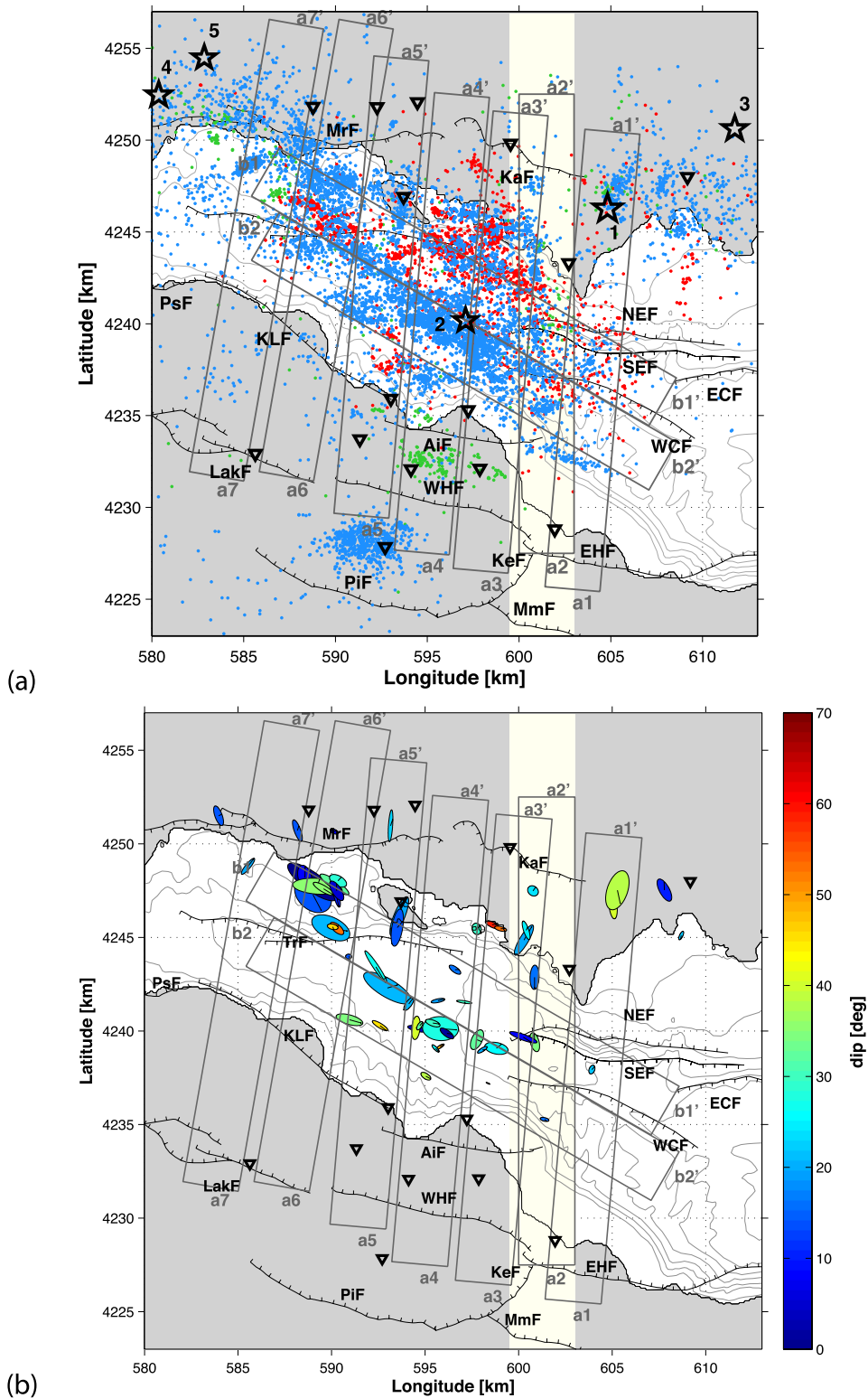


Figure 5. (a) Map of the relocated seismicity (blue: 2000–2007, red: 1995 and green: 1991). Stars correspond to large earthquakes ($M_s \geq 5.5$): 1: $M_s = 6.2$ 1995 Aigion earthquake (Bernard *et al.* 1997), 2: largest aftershock of 1995 Aigion earthquake ($M_1 = 5.2$), 3: 1997 Agios Pandes earthquake ($M_s = 5.3$), 4 and 5: 2010 Efpalio earthquakes (Sokos *et al.* 2012; $M_w = 5.3$ and $M_w = 5.2$). (b) Map of the largest multiplets. Each multiplet is represented by an ellipse. Colours correspond to the dip of the plane containing the ellipse and black lines to the downdip direction. Dark grey rectangular boxes correspond to cross-sections detailed in Figs 7–9. Main faults as in Fig. 1. Black triangles indicate stations used on the 2000–2007 period.

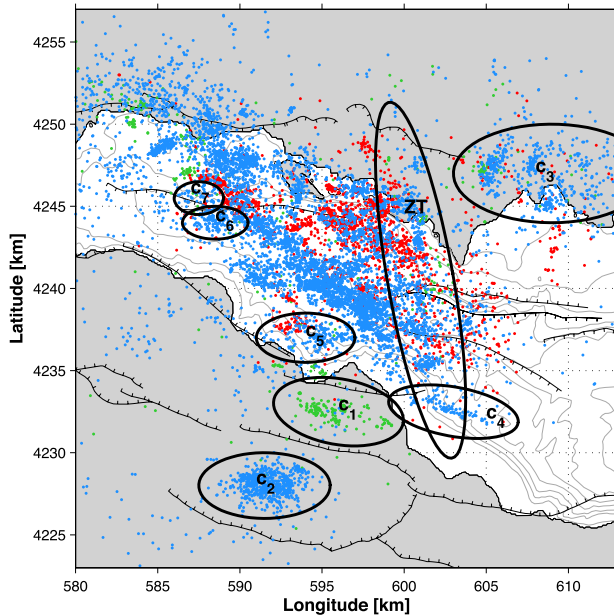


Figure 6. Location of the main clusters discussed in the text. Clusters are identified by black ellipses, and are labelled from c_1 to c_7 . ZT locates the transition zone. Colour codes and main faults are defined in Fig. 5.

distances (Figs 7–9). In the ZE, the seismicity rate is lower and the seismicity is mainly located below the northern coast at depth larger than 10 km (Figs 6 and 7, section a_1 , cluster c_3). The absence of seismicity shallower than 3.5–4 km depth makes it difficult to outline the geometry of faults at depth and to estimate their dips. On the southern coast, no background seismicity is observed, the seismicity is characterized by swarms concentrated in time and space: 2001 swarm (Fig. 6 cluster c_2) around station AIO (Pacchiani & Lyon-Caen 2010) and 1991 swarm (Fig. 6 cluster c_1) around station KOU/TEM (Rigo *et al.* 1996).

The geometries and the distribution of the large multiplets highlight the complexity of the seismicity structure beneath the rift, particularly in the centre of the rift (Figs 5 and 7, sections b_1 and b_2) and near station PYR (Fig. 9, section a_6), where the density of events is large. Multiplets have mainly north dipping geometries; they have relatively steep dips (30–50°) along the south coast at the root of the faults observed at the surface (Figs 8 and 9, sections a_2 – a_5 , multiplet clusters m_1 – m_4) and they have lower dips (10–20°) along the northern coast (same sections at distances larger than 15 km, multiplet clusters m_9 – m_{11}). A few multiplets have a south dipping geometry (Fig. 8, section a_3 , multiplet cluster m_5), or a subvertical geometry (Fig. 9, section a_6 , multiplet cluster m_8). Multiplets have mainly E–W strikes in agreement with the strike of the main faults (see Fig. 5, black lines in ellipses indicating downdip direction), and they are generally consistent with focal mechanisms computed in previous studies. For instance, multiplets at the northwestern limit of the area (Fig. 9, section a_7 , multiplet cluster m_7) are consistent with the shallow north dip (12–20°) obtained by Rietbrock *et al.* (1996). Multiplet geometries are also consistent with fault plane solutions from an unpublished work (Pacchiani 2006) and from Rigo *et al.* (1996), showing shallowly north dipping structures along and below the northern coast (Fig. 8 section a_2 , multiplet cluster m_{10} and Fig. 9 section a_5 , multiplet cluster m_9), subvertical microstructures (Fig. 9 section a_6 , multiplet cluster m_8) and structures with higher dips along the southern coast at the roots of the major faults (Fig. 8 section a_3 , multiplet cluster m_2 and section a_4 , multiplet cluster m_3).

After this general overview, we will now describe in more detail specific features of the different structures and areas identified thanks to the relocation process.

4.1 N–S striking ZT

As already mentioned, a difference in the seismicity pattern is observed between the ZE and the ZW of the studied area, respectively, the sectors (1) and (3) in Fig. 2. The two sectors are clearly separated by a thin NNW structure 1–3 km wide (Fig. 5, ivory coloured strip, and Fig. 8 section a_2 and grey coloured strip in Fig. 7 sections b_1 and b_2) shallowly dipping to the north (~ 22 – 23°) containing numerous multiplets (Fig. 8 section a_2 , multiplet cluster m_{10}). Hereafter, this structure will be called ‘Transition Zone’ (ZT in Fig. 2). The two EW sections (Fig. 7, sections b_1 and b_2) show that the seismicity has shallower depth around the ZT than further east and west, and forms a bell-like structure (Fig. 7 at distances of 12–20 km along sections).

4.2 Western zone (ZW)

In this zone, the seismicity is mainly located below the gulf, concentrated at 6–10 km depth in a 1- to 1.5-km-thick layer shallowly dipping to the north (Fig. 7 sections b_1 and b_2 , Fig. 8 sections a_2 – a_4 and Fig. 9 sections a_2 – a_7), supporting observations from previous studies (Rigo *et al.* 1996; Lyon-Caen *et al.* 2004; Bernard *et al.* 2006). The high-resolution relocation indicates that the structure of this layer is complex and highly variable along the rift. The deeper part is very thin (less than 0.1–0.3 km), gently dipping to the north (15–20°; Fig. 8, sections a_2 – a_4 and Fig. 9 section a_5 , at distances larger than 15 km along sections, multiplet clusters m_9 – m_{11}), and it contains well-defined multiplets elongated in the downdip direction (Fig. 5). In this part of the layer, the dips of the multiplets and the dip of the layer are similar (10–20°). The upper part is thicker (between 1 and 1.5 km) and flat (Fig. 8 section a_3 – a_4 and Fig. 9 section a_5 at distances of 10–15 km along section), and it contains numerous multiplets having variable strikes (220–310°) and larger dips (25–45°) than in the deeper part as well as multiplets without any planar geometries. In this part, the multiplets have larger dips than the general dip of the layer. The western edge of this layer (Fig. 9, sections a_6 and a_7) has a more complex structure, also with a large variability in multiplet geometries (strikes: 180–345°, dips: 15–45°). At depth, the seismic zone is delineated to the south by the roots of the north dipping ‘en echelon’ faults: the AiF, the KLF system and the PsF (Bernard *et al.* 2006).

4.2.1 Faults under the northern coast

Some historical earthquakes have struck the northern coast of the rift [see Fig. 1, Ambraseys & Jackson (1990); Papazachos & Papazachou (1997); Makropoulos *et al.* (2012)] in 1580, 1909 and 1965, but their locations are not well known, and the events cannot be clearly associated either to some of the minor antithetic faults identified at the surface (Gallousi & Koukouvelas 2007; Balkanliotis 2009), or to the main north dipping structures. The absence of seismicity down to 4 km depth makes it difficult to link seismicity at depth with faults at the surface. A few multiplets have a south dipping geometry (see multiplet cluster m_5 directly below the northern coastline between Trizonia island and the ZT, Figs 5 and 8, section a_3). These multiplets contain mainly events occurring in 2000. Some aftershocks of the 1995 Aigion event (Bernard

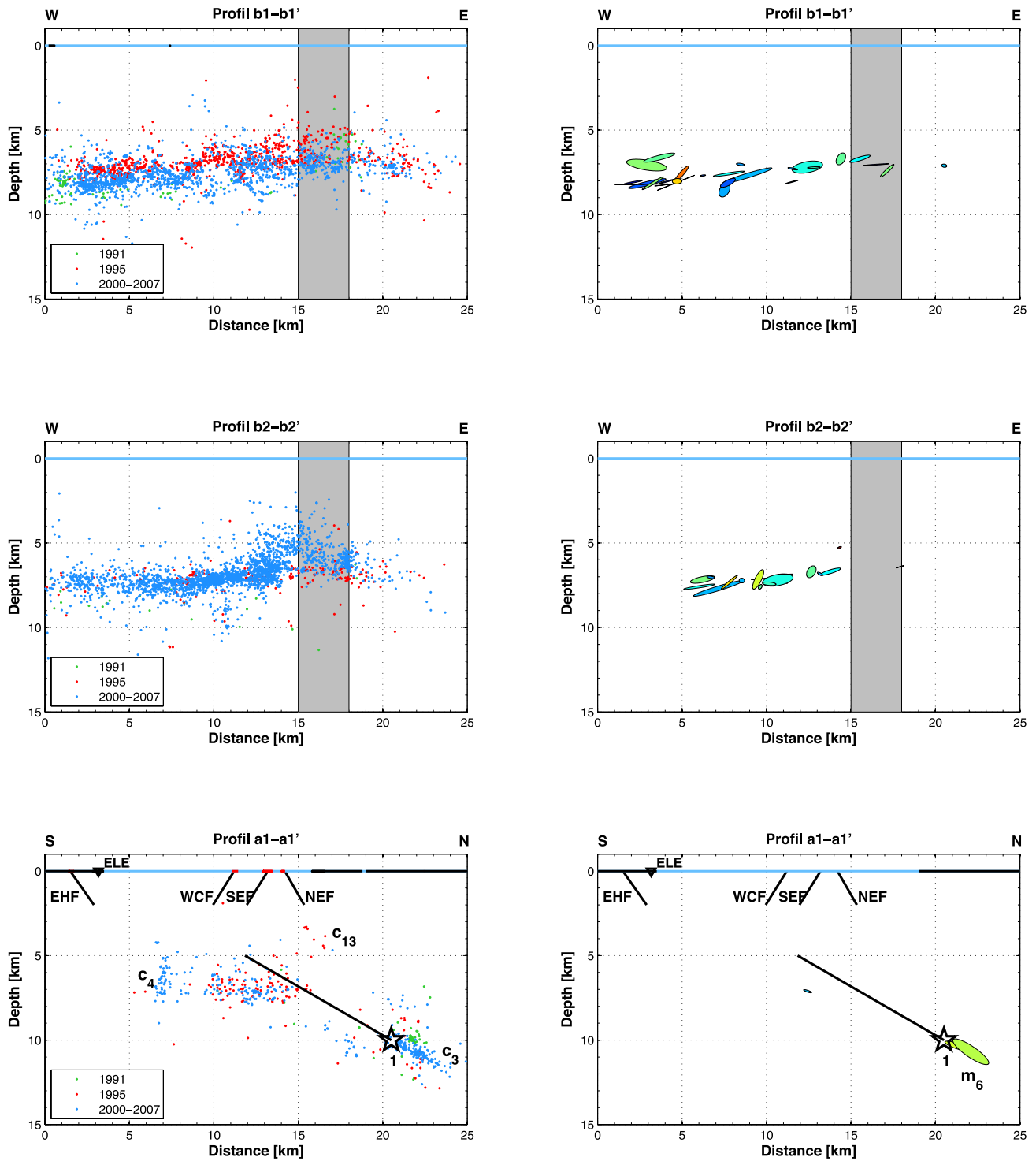


Figure 7. Detail of the cross-sections identified in Fig. 5 by grey rectangular boxes. Left-hand side: relocated seismicity, colours as in Fig. 5: blue for 2000–2007 seismicity, red for 1995 and green for 1991. Clusters discussed in the text are labelled c_n . Right-hand side: multiplet geometries. Multiplet groups discussed in the text are labelled m_n . Shaded grey strips indicate the location of the transition zone between the western and eastern parts of the studied area. Bold black lines indicate the major onshore and offshore faults. The 1995 rupture is shown in bold black. Stars correspond to large earthquakes as defined in Fig. 5. 1: $M_s = 6.2$ 1995 Aigion earthquake (Bernard *et al.* 1997). Light blue lines represent the offshore part of the rift.

et al. 1997) are also located in the same area, with similar geometries (red dots in Fig. 10, at distances 10–14 km along section). These multiplets and the relocated seismicity seem to highlight two subparallel south dipping structures (labelled k_1 and k_2 in Fig. 10)

on a narrow strip (1–2 km wide) near the ZT. Their dip at depth is about 45° . These structures are observed from 5 km down to 11 km depth, and therefore must be mature structures. The k_1 structure has been activated above the active layer only in 1995,

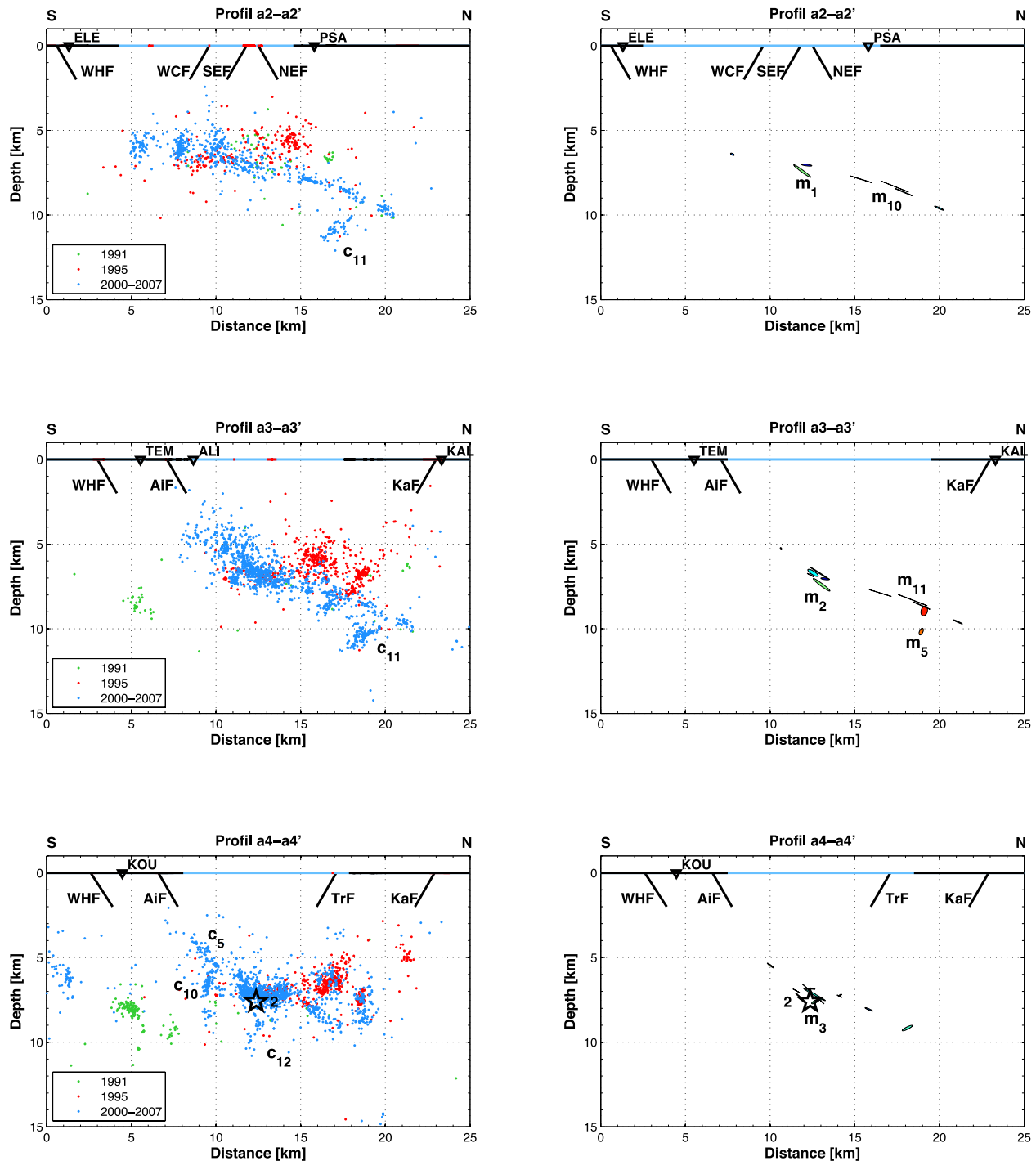


Figure 8. Detail of the cross-sections (*continued*). Stars correspond to large earthquakes as defined in Fig. 5, 2: largest aftershock of 1995 Aigion earthquake ($M_1 = 5.2$).

after the Aigion earthquake, and beneath the layer over the 2000–2007 period.

4.2.2 Southern faults: Pirgaki-Mamoussia and Kerinitis

The southern coast of the rift is characterized by the absence of background seismicity and the presence of several seismic swarms. Two significant swarms have been recorded during the observa-

tion periods, one in 1991 and one in 2001 (see Fig. 11). In 2001, a swarm occurred near station AIO (blue dots in Fig. 11), called the 2001 Agios Ioanis earthquake swarm (Lyon-Caen *et al.* 2004; Zahradnik *et al.* 2004; Pacchiani & Lyon-Caen 2010). The main shock of this sequence has a local magnitude of 4.3, its focal mechanism indicates normal faulting with a strong component of strike slip. It occurred on a 40° NW dipping fault, that can be associated to the Kerinitis Fault (KeF; Pacchiani & Lyon-Caen 2010). This fault is transverse to the main faults on the south coast, but

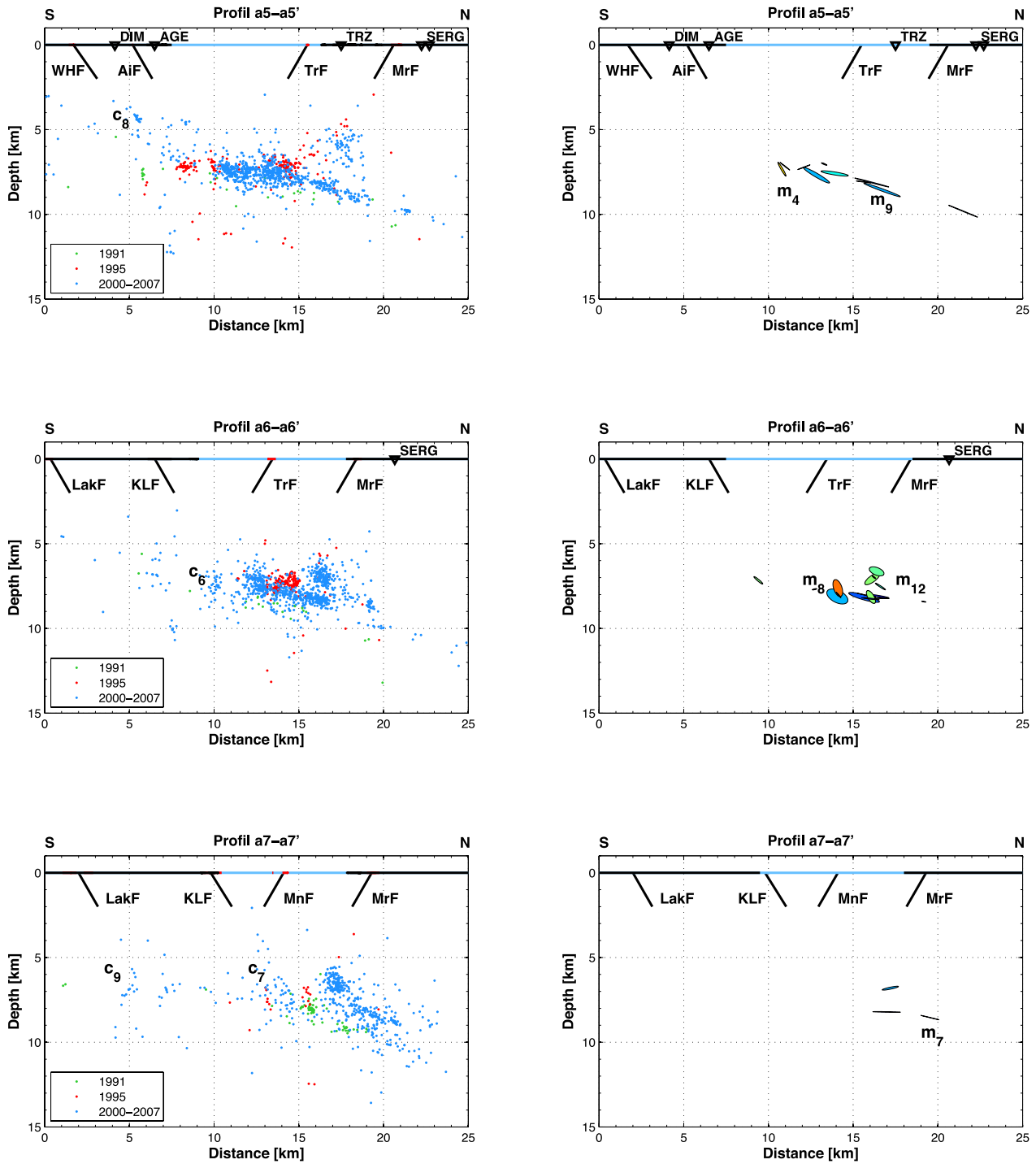


Figure 9. Detail of the cross-sections (continued).

the focal mechanism of the main shock is consistent with the NS extension.

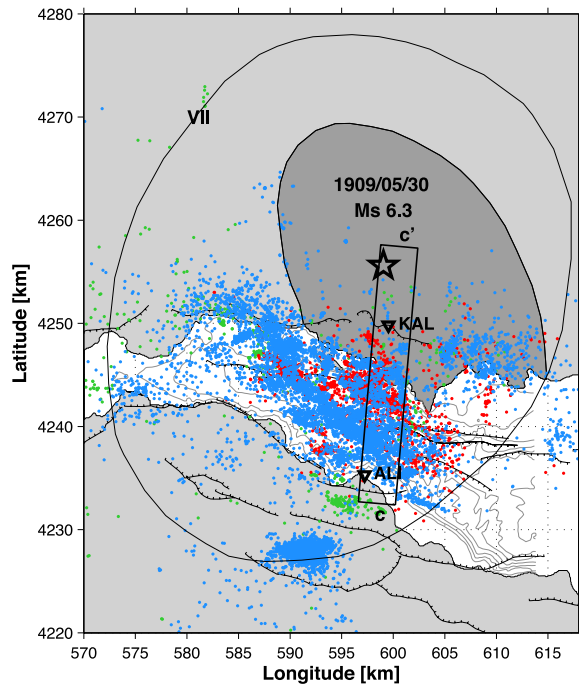
In 1991, a swarm occurred near stations KOU and TEM (green dots in Fig. 11). It was observed during the 2 months of the experiment (July and August), an $M_l = 4.5$ event occurred at the beginning of the swarm (1991 July 3; Rigo *et al.* 1996). Keeping only very well-located events, the seismicity is located between 7.5 and 9.5 km depth and seems to be north dipping ($40\text{--}45^\circ$) and E–W striking (see Figs 11 and 8 section a_4). The downdip extension of the

swarm is small, therefore it is difficult to assess the true geometry of the associated structure.

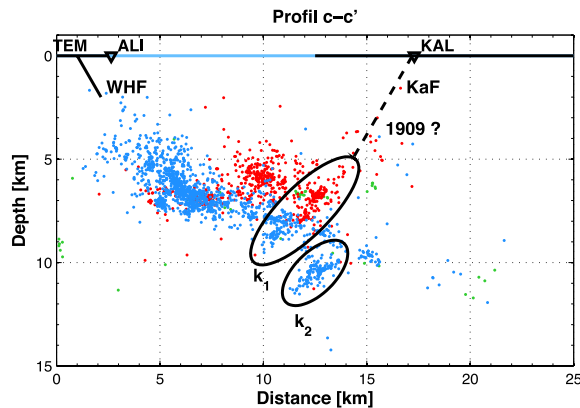
The relationship between these two clusters is further discussed in Section 6.

4.2.3 AiF and KLF system

The microseismicity clearly outlines the AiF up to 4.5–5 km depth (Fig. 8, section a_4 , cluster c_5). The dip of the structure is consistent



(a)



(b)

Figure 10. (a) Location map of the 1909 Fokis earthquake ($M_s = 6.3$) relative to the relocated seismicity (blue: 2000–2007, red: 1995, green: 1991). The dark grey area represents the zone of maximum damage. Black line corresponds to the intensity VII isoseist from Ambraseys & Jackson (1990). The star indicates the likely epicentre location of the event, it was arbitrarily located in the centre of the area of maximum damages. Main faults are indicated in black. (b) Detail of the cross-section indicated by a black rectangular box on the map. Two south dipping structures labelled k_1 and k_2 are indicated, they correspond to possible candidates for the fault at the origin of the 1909 earthquake. The preferred candidate is the Kalithea Fault (corresponding to structure k_1 and indicated by a black dashed line).

with the one observed at the surface $\sim 60^\circ$, also constrained by the 1-km-deep AIG10 borehole (Cornet *et al.* 2004) and consistent with the geometry of multiplets and their fault plane solutions (Godano *et al.*, submitted to *GGU*). The fault is rooting in the dense seismic layer. The KLF system is not clearly outlined by the seismicity over the period 2000–2007; a few events (cluster c_6 and c_7) on section a_6 and section a_7 (Fig. 9) may however be associated to the root of the fault system in the seismically active layer, in which case, the faults have dips around $50\text{--}60^\circ$. Recently, a swarm in 2009 clearly

outlines the root of the KLF system in the active layer indicating similar dips (Barnoud 2012).

Several structures 1–2 km long are observed below the AiF (Fig. 8 section a_4 , cluster c_{10}) and below the seismically active layer (Fig. 8 sections a_2 and a_3 cluster c_{11} , and section a_4 cluster c_{12}).

4.2.4 LakF and WHFs

A weak but clear activity can be observed between 4 and 7 km depth close to the WHF (Fig. 9 section a_5 cluster c_8). It may be associated to the WHF, and therefore its dip at depth is about 45° . The association with the LakF is less clear, because the seismicity is sparse: only few events on section a_7 (Fig. 9 cluster c_9) may correspond to the root of the LakF in the prolongation of the seismic active layer.

4.2.5 Offshore western faults

The two major mapped offshore faults are the TrF and MnF. Both are south dipping faults. None of these faults are clearly observed in the seismicity, even though they are clearly visible in the bathymetry. Indeed, the TrF has a 400-m-high fault scarp (Moretti *et al.* 2003), and the MnF has a smaller fault scarp, however it is still visible in the bathymetry. We note that a few events beneath the seismically active layer (Fig. 8 section a_4 cluster c_{12}) define a south dipping segment aligned with the TrF.

4.3 Eastern zone (ZE)

4.3.1 The EHF, and the 1995 rupture

In this part of the rift, most of the seismicity is located beneath the northern coast at depths larger than 10 km (Fig. 7 section a_1 cluster c_3). The seismicity is mainly structured along a shallowly north dipping plane including multiplets (multiplet cluster m_6) with dips ($\sim 30^\circ$) in agreement with the general slope. This structure matches very well the $M_s = 6.2$ 1995 Aigion earthquake rupture plane from Bernard *et al.* (1997). The 1995 event is the largest recorded in the rift since the 1981 sequence that occurred at the eastern edge of the rift (Jackson *et al.* 1982), and severely damaged the city of Aigion. A multidisciplinary study (Bernard *et al.* 1997) including seismological and geodetic analysis indicates that the preferred hypocentre is located below the northern coast and that the rupture started at a depth of 10 km ($38^\circ 21.7'N$, $22^\circ 12.0'E$) on an EW striking low-angle plane dipping to the north (strike 277° , dip 33° , rake -77°). It was followed by many aftershocks, in particular one of magnitude $M_1 = 5.2$ (star 2 on Figs 5 and 8 section a_4). Surprisingly, the aftershocks are mainly located in the western part of the rift, and not especially close to the rupture plane (Fig. 5, red dots). The aftershocks observed above the main seismically active layer (Fig. 10) are located close to the plane containing the 1995 rupture area, and shifted to the west. This aftershock zone is thus expected not to be in the stress shadow of the 1995 event, hence experiencing a large shear stress increase and small stress perturbation, consistent with a Coulomb stress increase.

4.3.2 Offshore eastern faults

In this part of the rift, three major offshore faults are mapped: the North and South Eratini faults and the West Channel Fault (respectively NEF, SEF and WCF on Fig. 1). All these faults are

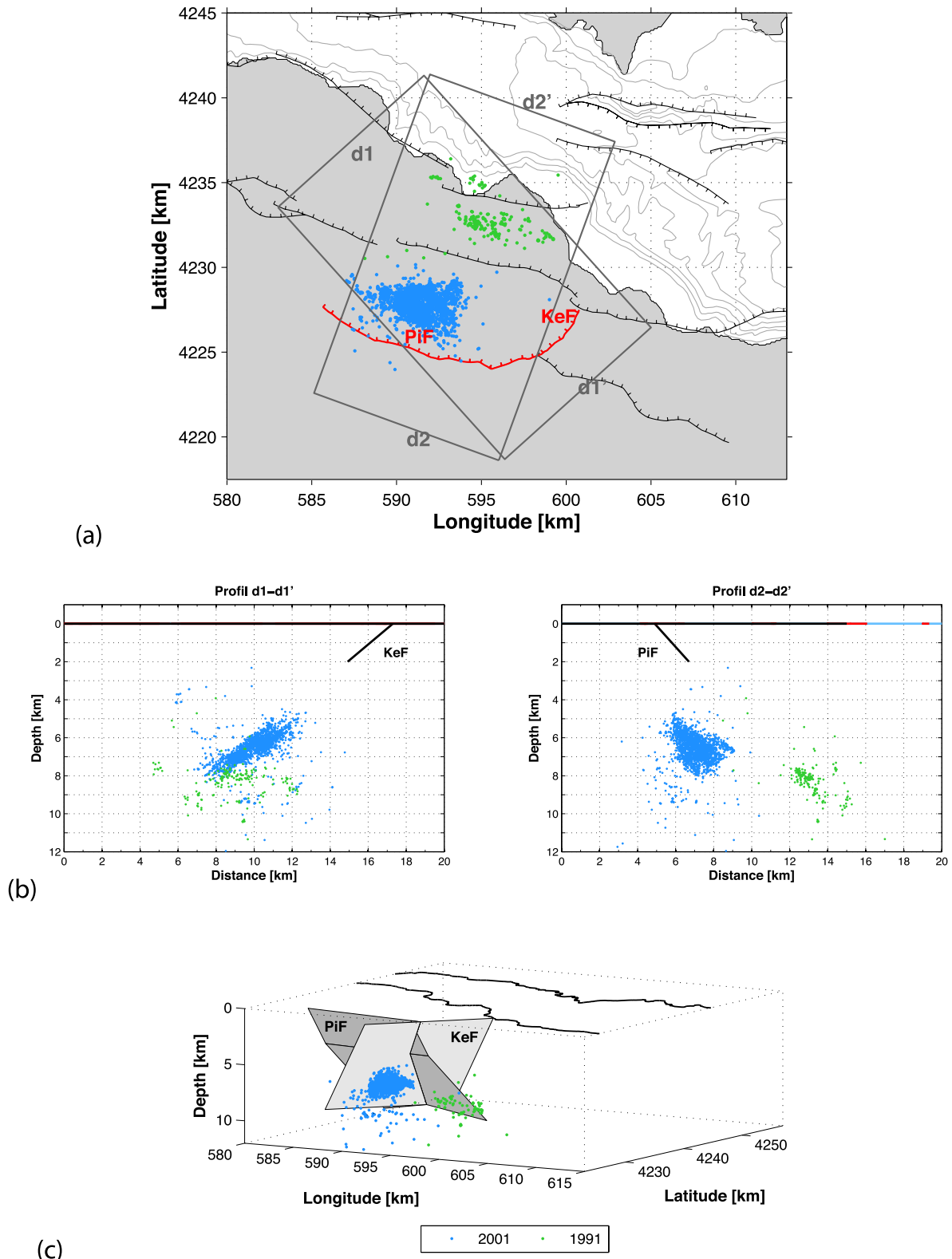


Figure 11. (a) Map of the relocation of the 2001 (blue) and 1991 (green) swarms. Main faults are indicated in black, the two faults which may be associated to these swarms are indicated in red: Pirkagi Fault (PiF) and Kerinitis Fault (KeF). (b) Detail of the two cross-sections indicated on the map by black rectangular boxes. The d1 cross-section is perpendicular to the KeF corresponding to the 2001 swarm. The section d2 is perpendicular to the major south dipping faults, in particular to Pirkagi Fault. (c) 3-D schematic view of the KeF and the PiF, and links to the two swarms: the 2001 swarm (blue) is associated to the KeF and the 1991 swarm (green) to the PiF.

well observed in the bathymetry and on seismic profiles (e.g. Bell *et al.* 2008, 2009; Taylor *et al.* 2011). There is no clear evidence of these faults in the seismicity, except some aftershocks of the 1995 event at 3.5–5 km depth, which may be associated to the North Eratini Fault (Fig. 7, section a_1 cluster c_{13}). A linear structure dipping 30° to the ESE is observed offshore close to stations TEM and ELE and the ZT (Fig. 7, section a_1 , cluster c_4). This structure is active over the whole time period 2000–2007, with numerous events in 2001 and 2002.

5 SPATIO-TEMPORAL VARIATION

In addition to the complexity of the structure described in the previous section, the space–time distribution of the seismicity also shows some interesting features. In this section, we present the most relevant results concerning the space–time distribution of the seismicity and discuss the mechanical implications for the large-scale deformation. An extensive study of the space–time evolution is beyond the scope of this paper. In order to highlight the spatio-temporal distribution of the seismicity, we consider four different areas (Fig. 12):

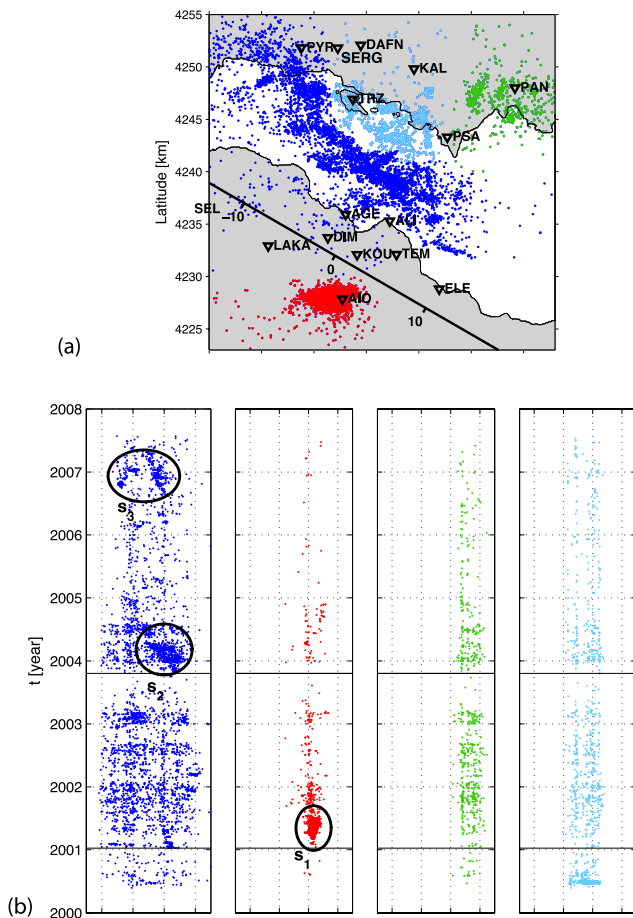


Figure 12. Spatio-temporal evolution of the seismicity. (a) Map presenting the four areas considered to explore the spatio-temporal evolution. Each colour corresponds to a different area. The black line corresponds to the direction of projection of the seismicity, the origin of the distance is indicated as well as ± 10 km. Stations are indicated by black inverted triangles. (b) Spatio-temporal variations of the seismicity along the projection direction for the four areas. Three clusters discussed in the text are indicated by black ellipses and labelled s_1 – s_3 , horizontal black lines indicate the start of two swarm activities discussed in the text.

one around station AIO, to the south, mainly corresponding to the 2001 swarm (red colour), one around station PAN (green colour) to the northeast, two in the centre of the rift (dark and light blue colours). We have divided the central part of the rift into two areas, to take into account the difference of structure of the active layer. In this analysis, the data from the two temporary experiments are not included. The distance is calculated along a N120°E direction (black line in Fig. 12), and all the events are projected onto this direction. We have also explored the distribution in a perpendicular direction, but the space–time evolution is less clear in this direction, because the reactivation of other areas (not the ones where the swarms occurred) is characterized by a small number of events compared to the number of events in the swarms. These results will not be presented here.

We first note a highly fluctuating seismicity level dominated by swarms, with some clear WNW–ESE diffusion in the central zone, at various space–time scales, as already reported by Bourouis & Cornet (2009). Three major swarms are identified (Fig. 12, clusters s_1 – s_3): one in 2001 near station AIO, one in 2003–2004 in the central part of the rift and one in 2006–2007 at the western end of the rift. These swarms are not mainshock–aftershock sequences: the event magnitude within these swarms ranges from 0.6 to, respectively, 4.5/3/3.5, the largest events occurring during the swarm activity, not at the beginning. We will not discuss in detail the diffusion pattern of these swarms as done in Bourouis & Cornet (2009), but we will focus on the comparison of the behaviour of the four identified areas of the rift.

We observe similar seismicity patterns in the four areas, a succession of seismically quiet and active periods at nearly the same time in the four areas. When a crisis occurs in an area of the rift, the three other areas are also slightly activated (increase of the event numbers), but with some time delay. We have identified two clear cases (and several others less clear) for which the seismic activity starts in the centre of the rift and spreads beneath the northern and the southern coasts. These two cases are underlined in Fig. 12 (horizontal black lines), and detailed in Fig. 13. The first example occurred in 2001: the activity started in the centre of the rift (dark blue), then spread to the north with delays of 5.7 and 9.5 d, respectively, for the part including TRZ (light blue) and the one including PAN (green) and finally to the south with a delay of about 21 d. In this case, the main part of the activity occurred in the south area. The second example occurred at the end of 2003 and beginning of 2004: the activity also started in the centre of the rift, then spread to the north with a delay of 14 d for the green area and finally to the south with a delay of 62.3 d. The area of the 2001 swarm was clearly reactivated at the end of 2003 and in 2004, when the swarm started in the centre of the rift (Figs 12 and 13).

The role of fluids in the observed seismicity pattern has already been suggested for a few specific cases (Bourouis & Cornet 2009; Pacchiani & Lyon-Caen 2010). The observations presented here suggest that fluids may, in large part, control the space–time evolution of the seismicity, through the non-stationary migration of pore pressure disturbances throughout the rift and a high connectivity between the four areas of the rift. As the delays are significantly larger for the southern part around station AIO, this suggests that this area is less well connected to the central rift zone than the other two. This may be understandable considering that this area is separated from the main rift zone by major tectonic structures. The large variation of seismicity rate over time is an important clue to the mechanical process, as we will see in the discussion section. The origin of these fluids remains an open question.

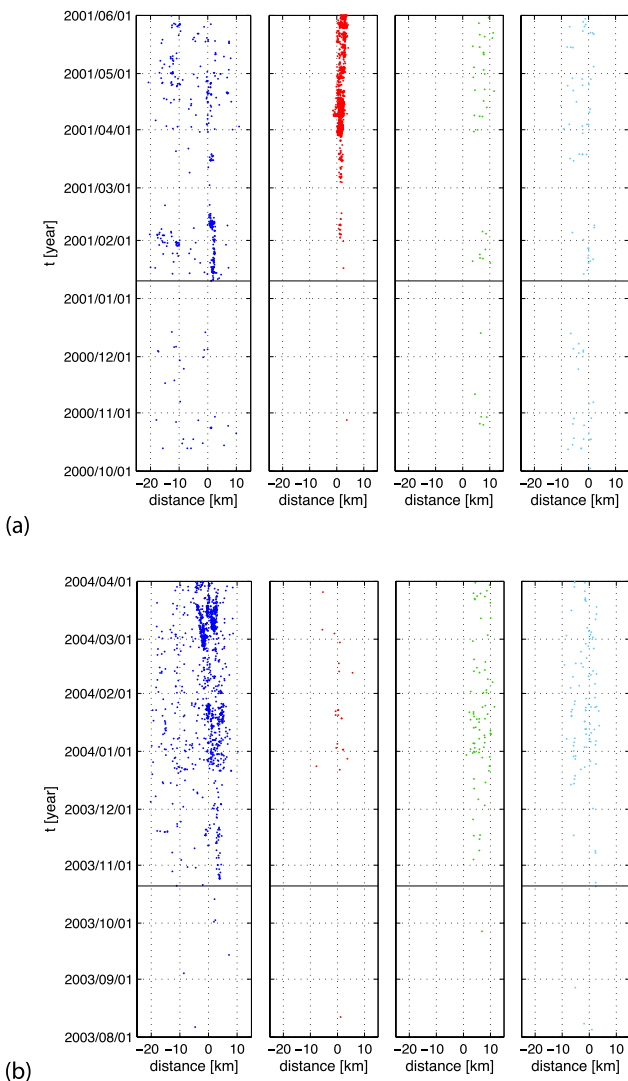


Figure 13. Details of the spatio-temporal variations for two reactivation episodes: (a) in 2001, and (b) in the end of 2003 and the beginning of 2004. Same as Fig. 12 for colours.

6 DISCUSSION

The high-resolution seismicity relocation that we obtained brings new insights into the seismicity structure at depth, the relationships with faults observed at the surface and the detailed microstructure of the seismogenic layer. After the detailed description of the seismicity structure in previous sections, we summarize here the observations and discuss their implications in terms of seismic hazard, possible association with the large earthquakes, general rift structure and mechanical process.

6.1 Seismicity and structure

6.1.1 The ZT

This structure is probably a main structural boundary, as it does not only delimit the seismicity pattern, but also some geomorphological structure of the rift. It indeed corresponds to: (1) a northward shift of the whole western fault system by about 10 km (Figs 1 and 2), at the transition between the AiF/TrF and the EHF/WCF—South and North Eratini (SEF, NEF) Fault system, (2) the western boundary of

the 1995 Aigion rupture plane (Bernard *et al.* (1997), star number 1 in Fig. 5), (3) the transition between the EHF and WHF, and (4) the presence of the transverse, NNE striking KeF. It also coincides with the transition between a narrow part of the rift with shallow bathymetry to the west, to an older, wider and deeper part to the east. The nature of this structure is not yet known, but it has the same orientation as the Hellenic nappes (e.g. Jolivet *et al.* 2010), and we suggest it may be controlled by inherited structures from these nappes.

6.1.2 The EHF, and the 1995 and 1861 ruptures

The 1861 December 26 earthquake is known to be related to the EHF as surface ruptures have been mapped (Schmidt 1881; Mouyaris *et al.* 1992). The maximum estimated intensity is IX-X, the on-land mapped rupture is 13 km long, and the estimated magnitude $M_w = 6.7$ (Papazachos & Papazachos 1980; Rigo 1994) considering a surface rupture of 325 km² and a mean displacement of 1 m. The 373 BC event (Mouyaris *et al.* 1992) likely occurred on the EHF as well. It seems to have larger magnitude than the 1861 one, and may have reactivated more than one segment with a magnitude probably closer to 7 (Papazachos & Papazachos 1980).

As already mentioned, the 1995 Aigion earthquake rupture started below the northern coast at 10 km depth on a low-angle plane dipping to the north at $\sim 33^\circ$ (Bernard *et al.* 1997).

As the seismicity rate is low to the east and no seismicity is observed above 5 km depth, the relationship between the 1995 rupture (Bernard *et al.* 1997) and the known normal faults at the surface is not obvious. This rupture may *a priori* be linked to one of the major north dipping faults: the AiF, the EHF or an offshore fault. Although damage is mainly observed in Aigion city (Bernard *et al.* 1997; Lekkas *et al.* 1998), the rupture is not associated to the AiF as it did not cross the ZT (Fig. 5). Thus, the rupture must be associated to the EHF, or to an offshore fault a few kilometres further north (Figs 14a and b). Seismic and bathymetric studies (Sachpazi *et al.* 2003; Bell *et al.* 2008; Taylor *et al.* 2011) do not identify the presence of major offshore faults that may correspond to the rupture, but as the rupture seems to have stopped or become significantly less active when reaching 4 km depth, the fault may possibly enter the thick sediments of the Gulf without reaching the seafloor. This fault geometry (Fig. 14a) implies a restraining step-over between the offshore fault and the EHF, where microseismicity is observed. If we consider a 45–50° dipping EHF disconnected from the rupture of the 1995 event, and possibly rooted down to 13 km without evidence of microseismic activity, the 1861 rupture would have occurred on a fault distinct from the one activated in 1995. In this model, the 1995 rupture is expected to have reduced the stress on the EHF.

Alternatively, to link the 1995 rupture to the EHF, we have to consider a smaller dip around 25–27° with a change of dip at a depth of 2–3 km to reach the 45–50° dip observed at the surface (Fig. 14b). Then, the EHF would form a single, major structure 20-km-long downdip, the 1861 having ruptured it entirely, or only its shallowest part. The 1995 event would then correspond to the rupture of an asperity on the deeper part of the Helike Fault, and would have increased the Coulomb stress on its upper part. Any new constraints on the geometry of the faults at depth is thus critical for seismic hazard assessment.

Seismological studies (Bernard *et al.* 1997) excluded very low dip angles (lower than 25°), and defined an acceptable dip range between 25° and 35°, which is consistent with the two competing

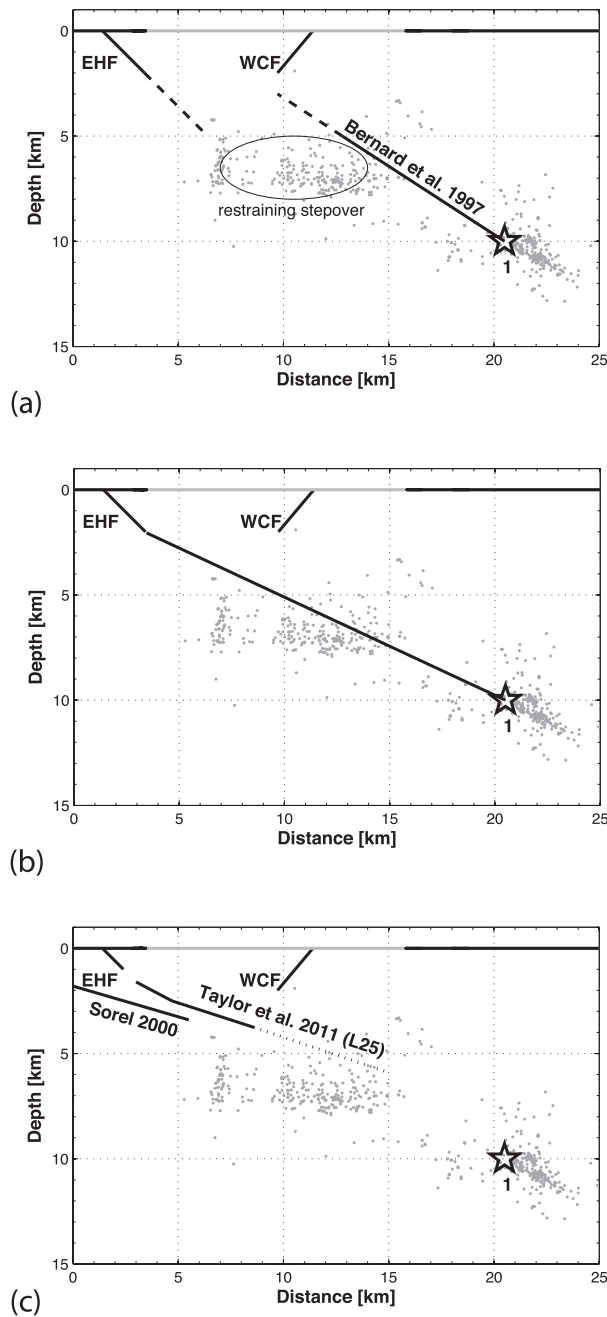


Figure 14. Possible scenarios for the 1995 rupture related to the East Helike Fault: (a) blind offshore fault, (b) deep part of the East Helike Fault (EHF), (c) fault geometries proposed by Sorel (2000) and Taylor *et al.* (2011). The seismicity is located at the western end of the EHF while the fault geometry proposed by Taylor *et al.* (2011) corresponds to its eastern end, however the location of the EHF onto the section is consistent for the both end of the fault. See text for detailed discussion. The relocated seismicity is in grey colour. Faults are indicated in black, the star corresponds to the epicentre of the $M_s = 6.2$ 1995 Aigion earthquake (Bernard *et al.* 1997).

schemes (Figs 14a and b). However, the GPS modelling favours the steepest dip range ($30\text{--}35^\circ$) to explain coseismic observations on the southern coast, in particular the ones near Aigion city (Bernard *et al.* 1997; Briole *et al.* 2000). Therefore, it favours the blind offshore fault hypothesis (Fig. 14a). Furthermore, the relocated seismicity and multiplets located at the root of the 1995 rupture at depths greater than 10 km have dips around 30° (Fig. 7 section a_1), which

is also more consistent with the offshore solution. Finally, in the model where the 1995 rupture would be linked to the deep part of the EHF (Fig. 14b), the microseismicity would be located mainly beneath the fault plane, and therefore it would be difficult to interpret it mechanically. Its location within the restraining step-over between the EHF and an offshore blind fault to the north is thus more consistent. In summary, although no microseismicity is observed on the 1995 main slip surface, we favour the blind offshore fault as the candidate for 1995 rupture.

From analyses of field observations, Sorel (2000) proposed a detachment with a dip of 20° , onto which EHF would root. This proposed detachment, when extrapolated further north falls well above the relocated seismicity and the 1995 hypocentre (Fig. 14c). Taylor *et al.* (2011) analysed several seismic profiles recorded offshore of the EHF, the relocated seismicity is to compare to their profile L27 located at the western end of the fault, however it is not close enough to the southern margin to image the fault, therefore we use the profile L25 located at the eastern end of the EHF for comparison, although the two profiles show significant differences in basin architecture. Taylor *et al.* (2011) proposed a biplanar fault geometry for the eastern end of the EHF: a dip of 35° from the surface down to about 2.5 km and a dip of 15° in its deeper part (Fig. 14c). This low-angle fault plane seems to have a different depth compared to the one proposed by Sorel (2000), however it is still above the relocated seismicity. Although its geometry is inferred from seismic profiles, the interpretation is questionable, as the reflectors may also correspond to the sediment/basement interface. The seismicity and the 1995 event are fundamentally incompatible with slip on such low-angle detachments.

To conclude, our relocated seismicity favours the scenario represented in Fig. 14(a), that is, a blind fault distinct from the EHF, however the other scenario (Fig. 14b) cannot be ruled out.

The relocated seismicity is mainly observed at the root of the 1995 rupture, nearly no seismicity is observed along the rupture plane before (1991) and after the 1995 event. Some more diffuse seismicity is located below the proposed 1995 rupture plane at 6–7 km depth (Fig. 7 section a_1). The seismicity at the root of the 1995 rupture defines a thin, planar structure, which one may relate to creep on the deepest part of the same fault. Its interpretation as the signature of a possible detachment will be discussed later. The 1995 patch is probably locked.

6.1.3 The central rift seismic zone

In the western part of the rift, the seismicity is concentrated in a seismically active layer at 6 to 10 km depth, with little seismicity above and below. The layer is flat in the centre of the rift, with a thickness between 1 and 1.5 km, and contains numerous multiplets with a wide range of strikes and dips (dips are larger than the dip of the layer itself), showing the internal complexity of the structure of this layer. Further to the north, the layer is thinner (0.1–0.3 km), slightly dipping to the north with a dip of $10\text{--}20^\circ$, and contains well-defined multiplets elongated in the downdip direction with dips consistent with that of the layer. Moreover, this seismically active layer has a high variability of internal structure and thickness along the rift over short distances.

The location of the microseismicity beneath the rift is consistent with the localization of the largest strain rate deduced from GPS studies (Briole *et al.* 2000; Avallone *et al.* 2004). In addition, the tomographic results (Latorre *et al.* 2004; Gautier *et al.* 2006, 2008) show high-velocity gradients at 5–7 km depth, interpreted as the

possible contact between two different units of the Hellenide orogenic belt: the Gavrovo–Tripolitza carbonate unit and the Phyllite series. The seismicity is located within an area characterized by low V_p/V_s and high V_p/V_s at 7–9 km depth, which may be indicators of a highly fractured medium and presence of fluids. All these observations are in agreement with the suggested role of fluids inferred from the spatio-temporal evolution of the microseismicity in the centre of the rift, with the high variability of multiplet geometries in the thicker part of the seismically active zone and with the presence of non-planar multiplets. They also indicate that the observed seismicity below the rift more likely corresponds to a layer of diffuse deformation than to a mature detachment.

6.1.4 Fault activity at depth

The obtained relocation allows a more detailed interpretation of major fault geometry and activity. The AiF roots into the seismically active layer at about 6 km depth, with a dip of 60°. Only its deeper part has microseismic activity, which may indicate that this part is creeping while the upper part is locked.

To the south, little seismicity is observed, except the 2001 swarm associated with the KeF, and the 1991 swarm. As the 1991 swarm is slightly deeper than the seismically active layer, it probably does not represent the continuation of the layer to the south (Fig. 8 section a_4). The two other candidates are the KeF and the PiF. The EW extension of the swarm (5 km long) is not in agreement with the KeF geometry. The swarm may thus be related to the deeper part of the PiF. In this case, the PiF intersects the KeF above the 2001 swarm, and may have acted as a barrier for the 2001 swarm slip (Fig. 11c). Some of the southern faults therefore seem not to be completely deactivated, but probably have low slip rates due to the northward migration of fault activities (Goldsworthy & Jackson 2001; Ford *et al.* 2012) in favour of the AiF and Kamarai–Lambiri Fault system (KLF). In fact, some seismicity is observed in the continuation of the active layer to the south, at the root of the WHF, and less clearly at the root of the LakF. These observations are consistent with the geological estimates by Pantosti *et al.* (2004) and Flotté (2003), who noted that the segment is no longer active or has extremely low slip rate. It is also consistent with the GPS observations showing no local deformation at the resolution of the GPS (10^{-7} ; Avallone *et al.* 2004).

Only few south dipping structures seem to be microseismically active. Some seismicity outlines two structures under the active layer (k_1 and k_2 in Fig. 10), one of which was partially activated in its upper part in 1995 (aftershocks of the Aigion earthquake). We suggest that the k_1 structure may be associated to the 1909 Fokis earthquake $M_s = 6.3$ (Ambraseys & Jackson 1990). This earthquake affected predominantly the northern coast between the Mornos river and the coast—a sparsely inhabited area—and caused extensive damage (see dark grey filled area in Fig. 10 identified as the area of maximum damage). The most probable fault associated with this earthquake is the Kalithea Fault (KaF) well observed at the surface, located close to the Kalithea station (KAL; dash black line in Fig. 10).

The TrF is not associated to any seismicity except below the active layer. This interpretation is consistent with the idea that the TrF could be deeply rooting, as it developed as an antithetic fault of the WHF.

The observed alignment in the ZE (Figs 6 and 7 cluster c_4) corresponds to the intersection at depth of the EHF and the WCF. Considering their known dips at surface—45–50° for EHF and 45–

60° for WCF (we will take 50° for both faults for computation)—and assuming that the dip does not change with depth, the intersection of the two faults should occur at about 5.7 km depth. This is consistent with the depth of the alignment. The slight eastward dip of this structure then suggests that both faults have slightly different strikes at depth. The WCF (1.5 Myr old) seems to have a low activity since 0.4 Myr (Bell *et al.* 2008), and may have been totally or partially deactivated due to the migration of the activity towards the north in favour of the SEF (0.5 Myr old). The EHF (0.7–1.1 Myr old) may have cut-off the WCF, and contributed to its deactivation. Some stress heterogeneities may be present at the intersection, which may explain the observed aligned seismicity.

For all the major faults observed at the surface or imaged in the bathymetric/seismic studies, an open question arises about whether these faults root in the seismically active layer or deeper in the crust. This has critical implications in terms of seismic hazard and maximum expected magnitude for events on these structures. As shown by the seismicity, the TrF, PiF and KaF seem to reach deeper than the active layer, but there is no evidence for the other faults.

6.2 Mechanical model

In the following, we show that some of the main results of the present work on the space–time distribution of microseismicity, when interpreted jointly with the results from 10 yr of continuous GPS measurements (<http://crlab.eu>), can lead to an alternative interpretation of the tectonic loading process of the active faults in this part of the Corinth Rift.

The standard model introduced by Rigo *et al.* (1996) is that the north dipping normal faults root within a low-dip angle, active detachment, subject to a stationary slip rate down to mid-crustal depths. Note that the slip on this detachment represents the integrated effect of the shear strain within the volume of the detachment layer. From the microseismic locations, in the central rift, this shear strain would be concentrated in a layer 1–2 km thick; further north and downdip, it may be 1 km or less; deeper than 12–15 km, it is silent and hence unresolved. Based on this, a kinematic model with uniform slip on the detachment is proposed by Briole *et al.* (2000) to fit the uniform velocities of the northern GPS points (sketch in model A in Fig. 15). However, a simple 2-D mechanical model (sketch in model B of Fig. 15) with stationary displacement rates at the northern and southern vertical boundaries of the model, and a stationary effective static friction coefficient on the surface representing the detachment, would produce slip values increasing towards the north—similar to crack models when moving away from the crack tip—and consequently would produce increasing velocities towards north within the northern crustal block. As this is not observed, model B is inadequate. Thus, a mechanical interpretation of model A implies a non-stationary effective friction of the detachment: one may propose that increasing damage in the microseismic layer, compatible with the many small-scale fault segments evidenced in our analysis, is responsible for an ongoing, effective weakening in the updip part of the detachment. In other words, this part of the detachment would be in a state of unstable failure, as it would release more strain per unit of time than what can be accumulated from the steady opening.

A direct consequence of model A is that the strain rate within the microseismic layer controls the surface velocity vectors at the GPS points on the northern coast. Thus, the evidence of constant GPS velocities for the last decade, with relative variations of less than 50 per cent at timescales greater than 6 months (see GPSCOPE

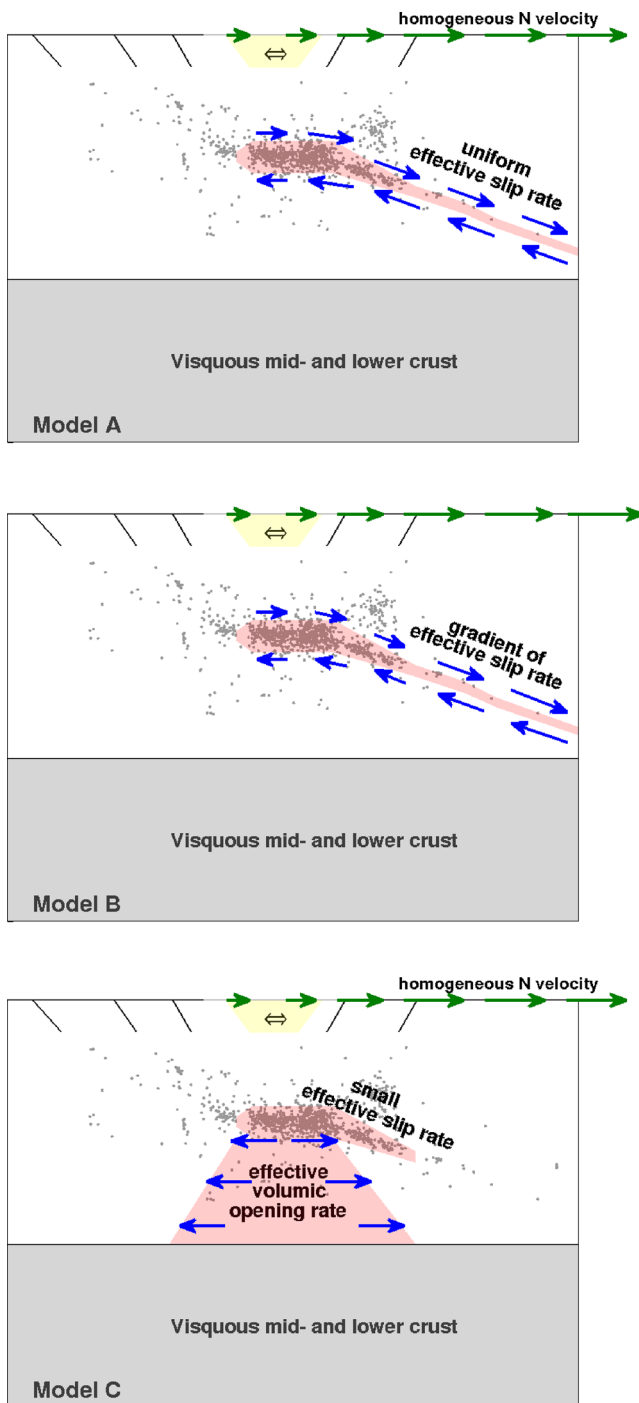


Figure 15. Proposed mechanical models to explain seismic and geodetic observations: (A) model with uniform slip on the detachment, (B) model with stationary displacement rates at the northern and southern vertical boundaries and a stationary effective static friction coefficient on the detachment and (C) model with a non-elastic opening below the rift axis. Green arrows are the horizontal velocity inferred from GPS. Black lines correspond to main faults. See detailed discussion of these models in the text.

web site), implies constant strain rates with similarly small relative variations. This is in contradiction with the large fluctuations of the seismicity rate, which can vary by a factor of 10 (1000 per cent), as reported above, if we assume the classical assumption of a proportionality between strain rate and seismicity rate

(e.g. Perfettini & Avouac 2004). Note that model B faces the same difficulty.

We therefore propose an alternative mechanical model (model C in Fig. 15): the opening of the western part of the rift would result from an hypothetical non-elastic opening below the rift axis. This horizontal stretching of the rift, below 8–10 km in depth, at about 10 mm yr^{-1} , would result from a lower effective viscosity or plasticity threshold, possibly due to the presence of fluids rising from the subducting slab, 50 km below, and would contribute to most of the opening rate measured at the surface from GPS. The measured stability of the surface velocities would thus simply reflect the stability of this opening strain rate at depth. In this model, the microseismic layer would represent the early stage of a detachment, growing downdip at a low angle towards the north, increasing in size at each major earthquake on its deepest part (like the 1995 event), leading in particular to the planar microseismicity structure in the continuation of the 1995 rupture area. The strong fluctuation of microseismicity would then be associated to rather small strain rate changes, undetected by the cGPS, as is suggested from local borehole dilatometer records (Canitano 2011). They could result from a non-linear response to the forcing steady strain from underneath, or could be triggered by non-stationary upward migration of fluid pulses from the middle crust. The fact that the perturbations of microseismicity seem to propagate from the centre of the rift outwards (see paragraph 4) is consistent with such a view. Also, the clear active structures imaged below the detachment (see sections a_2 – a_4 in Fig. 8) could be the signature of significant strain at these depths, favoured by model C.

For model C, in order to discuss the possible origin of this anelastic body in the deep central part, we first note that the internal forces within this body are not the driver of the rifting; the latter is mostly related to remote horizontal velocities of the elastic crust, to the north and to the south, as is assumed in most mechanical models for rifting (e.g. Pourhiet *et al.* 2003; Cianetti *et al.* 2008). This non-elastic body however influences the spatial distribution of the interseismic elastic strain in the rift, concentrating it upwards, thus explaining the strong NS gradient in GPS interseismic velocities. In that sense, at the surface, it acts similarly to the competing model of detachment (model B), for which the anelastic contribution comes from the slip on the detachment itself, leading to the same elastic strain concentration at its tip. Both models thus predict deficit in the released seismic moment of the rifting, if the latter is estimated using a standard, thick elastic crust (15 or 20 km) (Ambraseys & Jackson 1990; Clarke *et al.* 1997). We also note that the anelastic volume proposed in model C may keep an important elastic bulk, thus remaining in extension though with a smaller rate than above it, which could explain our observation of the deepest seismicity. The effective rheology of this microseismic layer may be due to low viscosity or plasticity, arising from high temperatures or specific rock composition, but may also result from the collective behaviour of an intensely fractured rock mass as suggested by the few deep microseismic structures of kilometric size (Fig. 8, clusters c_{11} and c_{12} in sections a_2 – a_4) possibly including near vertical faults and dykes with a significant opening component. Such fracturing and/or high temperatures may in particular arise from the effect of overpressurized fluids rising from the deeper crust. Following Bourouis & Cornet (2009), we propose that the subducting plate, 50 km beneath the western rift, may contribute to the fluid source through dehydration and serpentinization processes (Pearce *et al.* 2012), or as the subducted plate is old, the thick pile of sediments subducted with the plate may also be a source of fluids.

In conclusion, although we cannot rule out a major, low-angle detachment controlling the opening of the rift (model A), we show that an alternative model (C) with a centred, mode I-type opening of the rift might be plausible as well, and provides more consistent explanations for the space-time characteristics of the microseismicity reported in this paper. Further work with refined and new data analysis, as well as numerical mechanical modelling, such as the work recently initiated by Arem *et al.* (2012), are needed to better cross-evaluate the predictions of these two competing models, which have important consequences for a proper evaluation of long-term and time-dependent seismic hazard of this part of the rift.

7 CONCLUSION

Thanks to the high-precision relocation of seismicity, we have obtained a more detailed picture of the relationship between the seismicity at depth and the active faults at the surface. The AiF, the WHF, the LakF and the KLF system root in the seismically active layer at 6–8 km depth, with dips at depth similar to the ones observed at the surface. The WHF and LakF are not completely deactivated despite the northward migration of the fault system in favour of the younger Aigion–Kamarai–Lambiri Fault system, but they have probably a low slip rate. The KeF and the PiF are underlined, respectively, by the 2001 and 1991 swarms down to 7.5–8 and 8–9 km. The high precision relocation of the seismicity highlights, for the first time, some of the south dipping faults, bringing some constraints on their geometry at depth and their dips. The root of the TrF is probably observed under the seismically active layer with a dip of 60°, and the KaF has a dip of 45° in its deeper part.

We also obtain a more precise picture of the structure of the active seismic layer under the rift. Its shallow part is nearly horizontal, 1–1.5 km thick and contains multiplets with a high variability of geometries and higher dips than the layer itself; its deeper part is thinner (0.1–0.3 km), and contains well-organized multiplets with dips similar to the dip of the layer. The seismically active layer also has a high lateral variability of thickness and internal microstructures over short distances. This, together with the presence of seismic structures under the active layer, allows us to reject its interpretation as a major, mature detachment zone.

Combining information from GPS data and from the seismicity analysed in this study, we propose a new mechanical interpretation of the rifting process in the western part of the rift. The opening of the western rift would result from a non-elastic uniform deformation at depth under the rift axis, which would contribute most of the opening rate measured from GPS at the surface. The reported seismicity fluctuation would result from small strain rate changes, undetectable by the GPS, which could be triggered by the non-stationary migration of fluid pulses. The seismic layer dipping to the north would then represent an early stage of development of a detachment, not yet connected to the ductile middle crust, with an as-yet minor contribution to the rift opening.

This seismicity analysis also contributes to the knowledge of seismic hazard in the western part of the rift. The possibility of large slip in the central zone is unlikely, as the seismically active layer is not well structured. The understanding of the geometry of the EHF at depth, and of its link to the 1995 rupture is crucial for the seismic hazard in the area, as the 1995 rupture may have increased or decreased the Coulomb stress in the upper part of the EHF depending on various hypotheses. The seismicity analysis and the GPS data associated with the 1995 rupture favour the case in which the rupture decreased the Coulomb stress on the EHF, corresponding

to its occurrence along a fault distinct from the EHF. However, the other case cannot as yet be ruled out. As the WHF and LaF are not completely deactivated, but have probably low slip rate, a question arises concerning the seismic hazard associated to these faults. The south dipping Trizonia and Kalithea faults, highlighted in this study, are major structures: the 1909 earthquake possibly occurred on the Kalithea Fault, and the TrF might have a reduced potency for large ruptures. The understanding of their seismic potential is critical to the knowledge of the seismic hazard in the western part of the rift.

ACKNOWLEDGEMENTS

We thank all the persons which have been involved with CRLNET over the years and contributed to the existence of the data base exploited here, in particular: N. Germinis, F. Cornet, O. Lengliné, E. Sokos, A. Tselentis, P. Papadimitriou, N. Voulgaris, K. Makropoulos, J. Zahradnik and V. Plicka. We also thank participants to the ANR project SISCOR for numerous discussions, in particular M. Ford and N. Meyer for their insight on active faults in the western Corinth Rift and P. Briole for discussions on GPS observations. We are grateful to the two anonymous reviewers, and M. Ford whose comments helped to improve this manuscript. CRLNET has been supported by INSU CNRS in France, by the European Community through the CORSEIS and 3HAZ projects and by Agence Nationale de la Recherche with the Cattel@crl and SISCOR projects.

REFERENCES

- Abers, G.A., 2009. Slip on shallow-dipping normal faults, *Geology*, **37**(8), 767–768.
- Abers, G.A., Mutter, C.Z. & Fang, J., 1997. Shallow dips of normal faults during rapid extension: earthquakes in the Woodlark-D'Entrecasteaux rift system, Papua New Guinea, *J. geophys. Res.*, **102**(B7), 15301–15317.
- Ambraseys, N.N. & Jackson, J.A., 1990. Seismicity and associated strain of central Greece between 1890 and 1988, *Geophys. J. Int.*, **101**, 663–708.
- Arem, S.E., Lyon-Caen, H., Bernardi, P., Garaud, J.-D., Rolandone, F. & Briole, P., 2012. Influence of rheological and frictional slip properties on fault mechanics, deformation rates and localization phenomena: the Corinth Rift case, in *Proceedings of the EGU General Assembly*, Vienna, Austria, EGU2012-14477.
- Armijo, R., Meyer, B., King, G.C.P., Rigo, A. & Papanastassiou, D., 1996. Quaternary evolution of the Corinth rift and its implications for the late Cenozoic evolution of the Aegean, *Geophys. J. Int.*, **126**, 11–53.
- Avallone, A. *et al.*, 2004. Analysis of eleven years of deformation measured by GPS in the Corinth rift laboratory area, *C. R. Geosci.*, **336**, 301–311.
- Balkaniotis, S., 2009. Correlation of Neotectonic structures and seismicity in the broader area of Corinth Gulf (Central Greece), *PhD thesis*, Thessaloniki University.
- Barnoud, A., 2012. Etude détaillée de la crise sismique de 2009 dans l'ouest du rift de Corinthe (Grèce) par l'approche des multiplets, *Master thesis*, Strasbourg University.
- Battaglia, J., Thurber, C.H., Got, J.-L., Rowe, C.A. & White, R.A., 2004. Precise relocation of earthquakes following the 15 June 1991 eruption of Mount Pinatubo (Philippines), *J. geophys. Res.*, **109**, B07302, doi:10.1029/2003JB002959.
- Bell, R.E., McNeill, L.C., Bull, J.M. & Henstock, T.J., 2008. Evolution of the offshore western Gulf of Corinth, *GSA Bull.*, **120**, 156–178.
- Bell, R.E., McNeill, L.C., Bull, J.M., Henstock, T.J., Collier, R.E.L. & Leeder, M.R., 2009. Fault architecture, basin structure and evolution of the Gulf of Corinth rift, central Greece, *Basin Res.*, **21**, 824–855.
- Bernard, P. *et al.*, 1997. The $M_s = 6.2$, June 15, 1995 Aigion earthquake (Greece): evidence for low angle normal faulting in the Corinth rift, *J. Seismol.*, **1**, 131–150.

- Bernard, P. *et al.*, 2006. Seismicity, deformation and seismic hazard in the western rift of Corinth: new insights from the Corinth rift laboratory (CRL), *Tectonophysics*, **426**, 7–30.
- Bernard, P., Charara, R., Serpetsidaki, A., Briole, P. & Diagourtas, D., 2010. *Embedded Time Scales for Slip Transients on the Psathopyrgos Normal Fault, Western Rift of Corinth, Greece*, ESC.
- Billiris, H. *et al.*, 1991. Geodetic determination of tectonic deformation in central Greece from 1900 to 1988, *Nature*, **350**, 124–129.
- Boncio, P., Brozzetti, F. & Lavecchia, G., 2000. Architecture and seismotectonics of a regional low-angle normal fault zone in central Italy, *Tectonics*, **19**(6), 1038–1055.
- Bourouis, S. & Cornet, F.H., 2009. Microseismic activity and fluid fault interactions: some results from the Corinth rift laboratory (CRL), Greece, *Geophys. J. Int.*, **178**, 561–580.
- Briole, P. *et al.*, 2000. Active deformation of the Corinth rift, Greece: results from repeated global positioning system surveys between 1990 and 1995, *J. geophys. Res.*, **105**(B11), 25 605–25 625.
- Brozzetti, F., Boncio, P., Lavecchia, G. & Pace, B., 2009. Present activity and seismogenic potential of a low-angle normal fault system (Citta di Castello, Italy): constraints from surface geology, seismic reflection data and seismicity, *Tectonophysics*, **463**, 31–46.
- Canitano, A., 2011. Analyse des influences externes et internes sur les mesures extensométrique en forage dans le Rift de Corinthe (Grèce), *PhD thesis*, Institut de Physique du Globe, France.
- Carmona, E., Almendros, J., Pena, J.A. & Ibanez, J.M., 2010. Characterization of fracture systems using precise array locations of earthquake multiplets: an example at Deception Island volcano, Antarctica, *J. geophys. Res.*, **115**, B06309, doi:10.1029/2009JB006865.
- Chiaraluce, L., Chiarabba, C., Collettini, C., Piccinini, D. & Cocco, M., 2007. Architecture and mechanics of an active low-angle normal fault: Alto Tiberina fault, northern Apennines, Italy, *J. geophys. Res.*, **112**, B10310, doi:10.1029/2007JB005015.
- Cianetti, S., Tinti, E., Giunchi, C. & Cocco, M., 2008. Modelling deformation rates in the western Gulf of Corinth: rheological constraints, *Geophys. J. Int.*, **174**, 749–757.
- Clarke, P.J. *et al.*, 1997. Geodetic estimate of seismic hazard in the Gulf of Korinthos, *Geophys. Res. Lett.*, **24**, 1303–1306.
- Cociani, L., Bean, C.J., Lyon-Caen, H., Pacchiani, F. & Deschamps, A., 2010. Coseismic velocity variations caused by static stress changes associated with the 2001 Mw-4.3 Agios Ionis earthquake in the Gulf of Corinth, Greece, *J. geophys. Res.*, **115**, B07313, doi:10.1029/2009JB006859.
- Collettini, C., 2011. The mechanical paradox of low-angle normal faults: current understanding and open questions, *Tectonophysics*, **510**, 253–268.
- Cornet, F.H., Doan, M.L., Moretti, I. & Borm, G., 2004. Drilling through the active Aigion fault: the AIG10 well observatory, *C. R. Geosci.*, **336**, 395–406.
- Deichmann, N. & Garcia-Fernandez, M., 1992. Rupture geometry from high-precision relative hypocentre locations of microearthquake clusters, *Geophys. J. Int.*, **110**, 501–517.
- Doutsos, T. & Poulimenos, G., 1992. Geometry and kinematics of active faults and their seismotectonic significance in the western Corinth-Patras rift (Greece), *J. Struct. Geol.*, **14**(6), 689–699.
- Efron, B., 1982. *The Jackknife, the Bootstrap, and Other Resampling Plans*, SIAM.
- Efron, B. & Tibshirani, R.J., 1993. *An Introduction to the Bootstrap*, Chapman and Hall.
- Fehler, M., House, L. & Kaieda, H., 1987. Determining planes along which earthquakes occur: method and application to earthquakes accompanying hydraulic fracturing, *J. geophys. Res.*, **92**(B9), 9407–9414.
- Flotté, N., 2003. Caractérisation structurale et cinématique d'un rift sur détachement: Le Rift de Corinthe-Patras, Grèce, *PhD thesis*, Université Paris-Sud.
- Ford, M., Rohais, S., Williams, E.A., Bourlange, S., Jousselin, D., Backert, N. & Malartre, F., 2012. Tectono-sedimentary evolution of the western Corinth rift (central Greece), *Basin Res.*, **25**, 3–25.
- Frémont, M.-J. & Malone, S.D., 1987. High precision relative locations of earthquakes at Mount St Helens, Washington, *J. geophys. Res.*, **92**, 10 223–10 236.
- Gallouci, C. & Koukouvelas, I.K., 2007. Quantifying geomorphic evolution of earthquake-triggered landslides and their relation to active normal faults. An example from the Gulf of Corinth, Greece, *Tectonophysics*, **440**, 85–104.
- Gautier, S., Latorre, D., Virieux, J., Deschamps, A., Skarpelos, C., Sotiriou, A., Serpetsidaki, A. & Tselentis, A., 2006. A new passive tomography of the Aigion area (Gulf of Corinth, Greece) from the 2002 dataset, *Pure Appl. Geophys.*, **163**, 431–453.
- Gautier, S., Nolet, G. & Virieux, J., 2008. Finite-frequency tomography in the crustal environment: application to the western part of the Gulf of Corinth, *Geophys. Prospect.*, **56**, 493–503.
- Geller, R.J. & Mueller, C.S., 1980. Four similar earthquakes in central California, *Geophys. Res. Lett.*, **7**, 821–824.
- Ghiesetti, F. & Vezzani, L., 2004. Plio-pleistocene sedimentation and fault segmentation in the gulf of Corinth (Greece) controlled by inherited structural fabric, *C. R. Geosci.*, **336**, 243–249.
- Ghiesetti, F. & Vezzani, L., 2005. Inherited structural controls on normal fault architecture in the Gulf of Corinth (Greece), *Tectonics*, **24**, TC4016, doi:10.1029/2004TC001696.
- Godano, M., Deschamps, A., Lambotte, S., Lyon-Caen, H. & Bernard, P., 2012. Focal mechanisms of earthquake multiplets in the western part of the Corinth rift (Greece), in *Proceedings of the EGU General Assembly, Session: Open Session on Seismology; 14:EGU2012-5485*. Vienna, Austria.
- Goldsworthy, M. & Jackson, J., 2001. Migration of activity within normal fault systems: examples from the quaternary of mainland Greece, *J. Struct. Geol.*, **23**, 489–506.
- Got, J.-L., Frechet, J. & Klein, F., 1994. Deep fault plane geometry inferred from multiplet relative relocation beneath the south flank of Kilauea, *J. geophys. Res.*, **99**, 15 375–15 386.
- Hatzfeld, D. *et al.*, 1996. The Galaxidi earthquake of 18 November 1992: a possible asperity within the normal fault system of the Gulf of Corinth (Greece), *Bull. seism. Soc. Am.*, **86**(6), 1987–1991.
- Hatzfeld, D., Karakostas, V., Ziazia, M., Kassaras, I., Papadimitriou, E., Makropoulos, K., Voulgaris, N. & Papaioannou, C., 2000. Microseismicity and faulting geometry in the Gulf of Corinth (Greece), *Geophys. J. Int.*, **141**, 438–456.
- Hauksson, E. & Shearer, P., 2005. Southern California hypocenter relocation with waveform cross-correlation, part 1: results using the double difference method, *Bull. seism. Soc. Am.*, **95**, 896–903.
- Jackson, J.A., Gagnepain, J., Houseman, G., King, G.C.P., Papadimitriou, P., Soufleris, C. & Virieux, J., 1982. Seismicity, normal faulting and the geomorphological development of the Gulf of Corinth (Greece): the Corinth earthquakes of February and March 1981, *Earth planet. Sci. Lett.*, **57**, 377–397.
- Johnson, R.A. & Loy, K.L., 1992. Seismic reflection evidence for seismogenic low-angle faulting in southeastern Arizona, *Geology*, **20**, 597–600.
- Jolivet, L., Labrousse, L., Agard, P., Lacombe, O., Bailly, V., Lecomte, E., Mouthereau, F. & Mehl, C., 2010. Rifting and shallow-dipping detachments, clues from the Corinth rift and the Aegen, *Tectonophysics*, **483**, 287–304.
- Kapetanidis, V. & Papadimitriou, P., 2011. Estimation of arrival-times in intense seismic sequences using a master-events methodology based on waveform similarity, *Geophys. J. Int.*, **187**, 889–917.
- Latorre, D., Virieux, J., Monfret, T. & Lyon-Caen, H., 2004. Converted seismic wave investigation in the Gulf of Corinth from local earthquakes, *C. R. Geosci.*, **336**, 259–267.
- Lecomte, E., Pourhiet, L.L. & Lacombe, O., 2012. Mechanical basis for slip along low-angle normal faults, *Geophys. Res. Lett.*, **39**, L03307, doi:10.1029/2011/GL050756.
- Lee, W.H.K. & Lahr, J.C., 1972. A computer program for determining hypocenter, magnitude, and RST motion pattern of local earthquakes. Open-le Rep 75-311, U.S. Geol. Surv.
- Lekkas, E.L., Lozios, S.G., Skourtsos, E.N. & Kranis, H.D., 1998. Egio earthquake (15 June 1995): an episode in the neotectonic evolution of Corinthiakos gulf, *J. Geodyn.*, **26**, 487–499.
- Lyon-Caen, H., Papadimitriou, P., Deschamps, A., Bernard, P., Makropoulos, K., Pacchiani, F. & Patau, G., 2004. First results of the CRLN seismic

- array in the western Corinth Gulf: evidence for old fault reactivation, *C. R. Geosci.*, **336**, 343–351.
- Makropoulos, K., Kaviris, G. & Kouskouna, V., 2012. A updated and extended earthquake catalogue for Greece and adjacent areas since 1900, *Nat. Hazards Earth Syst. Sci.*, **12**, 1425–1430.
- Monigle, P.W., Nabelek, J., Braunmiller, J. & Carpenter, N.S., 2012. Evidence for low-angle normal faulting in the pumqu-xianza rift, Tibet, *Geophys. J. Int.*, **190**, 1335–1340.
- Moretti, I., Sakellariou, D., Lykousis, V. & Micarelli, L., 2003. The Gulf of Corinth: and active half graben? *J. Geodyn.*, **36**, 323–340.
- Moriya, H., Niitsuma, H. & Bayia, R., 2003. Multiplet-clustering analysis reveals structural details within the seismic cloud at the Soultz geothermal field, France, *Bull. seism. Soc. Am.*, **93**, 1606–1620.
- Mouyaris, N., Papastamatiou, D. & Vita-Finzi, C., 1992. The Helice fault, *Terra Nova*, **4**, 124–129.
- Nadeau, R.M. & Johnson, L.R., 1998. Seismological studies at Parkfield VI: moment release rates and estimates of source parameters for small repeating earthquakes, *Bull. seism. Soc. Am.*, **88**, 790–814.
- Ori, G., 1989. Geologic history of the extensional basin of the Gulf of Corinth (miocene–pleistocene), Greece, *Geology*, **17**, 918–921.
- Pacchiani, F., 2006. Etude sismologique des failles normales actives du Rift de Corinthe, *PhD thesis*, Université Paris XI.
- Pacchiani, F. & Lyon-Caen, H., 2010. Geometry and spatio-temporal evolution of the 2001 Agios Ioanis earthquake swarm (Corinth Rift, Greece), *Geophys. J. Int.*, **180**, 59–72.
- Palyvos, N., Pantosti, D., Martini, P.M.D., Lemeille, F., Sorel, D. & Pavlopoulos, K., 2005. The Aigion-Neos Erineos coastal normal fault system (western Corinth Gulf rift, Greece): geomorphological signature, recent earthquake history, and evolution, *J. geophys. Res.*, **110**, doi:10.1029/2004JB003165.
- Pantosti, D., Martini, P.M.D., Koukouvelas, I., Stamatopoulos, L., Palyvos, N., Pucci, S., Lemeille, F. & Pavlides, S., 2004. Paleoseismological investigations of the Aigion fault (Gulf of Corinth, Greece), *C. R. Geosci.*, **336**, 335–342.
- Papazachos, B. & Papazachos, C., 1980. *Seismicity of Greece*, Kluwer Press.
- Papazachos, B. & Papazachou, K., 1997. *Earthquakes in Greece*, Ekdoseis Ziti.
- Pearce, F.D., Rondenay, S., Sachpazi, M., Charalampakis, M. & Royden, L.H., 2012. Seismic investigation of the transition from continental to oceanic subduction along the western Hellenic subduction zone, *J. geophys. Res.*, **117**, doi:10.1029/2011JB009023.
- Perfettini, H. & Avouac, J.-P., 2004. Stress transfer and strain rate variations during the seismic cycle, *J. geophys. Res.*, **109**, doi:10.1029/2003JB002917.
- Poupinet, G., Ellsworth, W.L. & Frechet, J., 1984. Monitoring velocity variations in the crust using earthquake doublets: an application to the Calaveras fault, California, *J. geophys. Res.*, **89**(B7), 5719–5731.
- Pourhiet, L.L., Burov, E. & Moretti, I., 2003. Initial crustal thickness geometry controls on the extension in a back arc domain: case of the Gulf of Corinth, *Tectonics*, **22**, doi:10.1029/2002TC001433.
- Rice, J., 1992. Fault stress states, pore pressure distributions, and the weakness of the San Andreas fault, in *Fault Mechanics and Transport Properties in Rocks*, pp. 475–503, eds Evans, B. & Wong, T.F., Academic Press.
- Rietbrock, A., Tiberi, C., Scherbaum, F. & Lyon-Caen, H., 1996. Seismic slip on a low angle normal fault in the Gulf of Corinth: evidence from high-resolution cluster analysis of microearthquakes, *Geophys. Res. Lett.*, **23**(14), 1817–1820.
- Rigo, A., 1994. Etude sismotectonique et géodésique du golfe de Corinthe (Grèce), *PhD thesis*, University Paris 7, France.
- Rigo, A., Lyon-Caen, H., Armijo, R., Deschamps, A., Hatzfeld, D., Makropoulos, K., Papadimitriou, P. & Kassaras, I., 1996. A microseismic study in the western part of the Gulf of Corinth (Greece): implications for large-scale normal faulting mechanisms, *Geophys. J. Int.*, **126**, 663–668.
- Rohais, S., Eschard, R., Ford, M., Guillocheau, F. & Moretti, I., 2007. Stratigraphic architecture of the plio-pleistocene infill of the Corinth rift: implications for its structural evolution, *Tectonophysics*, **440**, 5–28.
- Rubin, A.M., Gillard, D. & Got, J.L., 1999. Streaks of microearthquakes along creeping faults, *Nature*, **400**, 635–641.
- Sachpazi, M., Clément, C., Laigle, M., Hirn, A. & Roussos, N., 2003. Rift structure, evolution, and earthquakes in the Gulf of Corinth, from reflection seismic images, *Earth planet. Sci. Lett.*, **216**, 242–257.
- Schaff, D.P., Bokelmann, G. H.R., Ellsworth, W.L., Znerkia, E., Waldhauser, F. & Beroza, G.C., 2004. Optimizing correlation techniques for improved earthquake location, *Bull. seism. Soc. Am.*, **94**(2), 705–721.
- Schmidt, J.F.J., 1881. *Studien über Vulkans und Erdbeben*, C. Scholtze.
- Smith, R.B., Navy, W.C., Julander, K.A., Viveiros, J.J., Baker, C.A. & Gants, D.G., 1989. Geophysical and tectonic framework of the eastern basin and range–Colorado plateau–rocky mountain transition, *Mem. Geol. Soc. Am.*, **172**, 205–233.
- Sokos, E. et al., 2012. The January 2010 Efpalio earthquake sequence in the western Corinth gulf (Greece), *Tectonophysics*, **530–531**, 299–309.
- Sorel, D., 2000. A pleistocene and still-active detachment fault and the origin of the Corinth–Patras rift, Greece, *Geology*, **28**(1), 83–86.
- Soter, S. & Katsonopoulou, D., 1999. Occupation horizons found in the search for the ancient Greek city of Helike, *Geoarchaeology*, **14**, 531–563.
- Stefatos, A., Papatheodorou, G., Ferentinos, G., Leeder, M. & Collier, R., 2002. Seismic reflection imaging of active offshore faults in the Gulf of Corinth: their seismotectonic significance, *Basin Res.*, **14**, 487–502.
- Stewart, I., 1996. Holocene uplift and paleoseismicity on the Eliki Fault, western Gulf of Corinth, Greece, *Annali di Geofisica*, **39**, 575–588.
- Taylor, B., Goodliffe, A.M. & Martinez, F., 1999. How continents break up: insights from Papua New Guinea, *J. geophys. Res.*, **104**, 7497–7512.
- Taylor, B., Weiss, J.R., Goodliffe, A.M., Sachpazi, M., Laigle, M. & Hirn, A., 2011. The structures, stratigraphy and evolution of the Gulf of Corinth rift, Greece, *Geophys. J. Int.*, **185**, 1189–1219.
- Tsujiura, M., 1983. Characteristic frequencies for earthquake families and their tectonic implications: evidence from earthquake swarms in the Kanto district, Japan, *Pure appl. Geophys.*, **121**, 573–600.
- Vidale, J.E., Ellsworth, W.L., Cole, A. & Marone, C., 1994. Variations in rupture process with recurrence interval in repeated small earthquake, *Nature*, **368**, 624–626.
- Waldhauser, F. & Ellsworth, W.L., 2000. A double-difference earthquake location algorithm: method and application to the northern Hayward fault, *Bull. seism. Soc. Am.*, **90**(6), 1353–1368.
- Waldhauser, F. & Schaff, D.P., 2008. Large-scale relocation of two decades of northern California seismicity using cross-correlation and double-difference methods, *J. geophys. Res.*, **113**, doi:10.1029/2007JB005479.
- Wernicke, B., 1995. Low-angle normal faults and seismicity: a review, *J. geophys. Res.*, **100**(B10), 20 159–20 174.
- Wyss, M., Pacchiani, F., Deschamps, A. & Patau, G., 2008. Mean magnitude variations of earthquakes as a function of depth: different crustal stress distribution depending on tectonic setting, *Geophys. Res. Lett.*, **35**(1), doi:10.1029/2007GL031057.
- Zahradnik, J., Jansky, J., Sokos, E., Serpetsidaki, A., Lyon-Caen, H. & Papadimitriou, P., 2004. Modeling the $M_1=4.7$ mainshock of the February–July 2001 earthquake sequence in Aegion, Greece, *J. Seismol.*, **8**, 246–257.

APPENDIX A: MULTIPLIET DETAILED INFORMATION

Table A1. Characteristics and geometry of the biggest multiplets: identification number of the multiplet (Id), number of events in the multiplets, date of the first and last events of the multiplet, mean location of the multiplet (latitude, longitude and depth), ellipse parameters (strike, dip, major and minor lengths: a_1 and a_2).

Id	nb events	Begin	End	Lat (°)	Lon (°)	Depth (km)	str (°)	dip (°)	a_1 (km)	a_2 (km)
19	40	2000/06/29	2000/07/11	38.35719	22.12836	8.950	127 ± 0	61 ± 1	0.429 ± 2	0.268 ± 1
1253	9	2001/09/21	2007/04/02	38.35290	22.06630	8.096	346 ± 0	35 ± 1	0.441 ± 2	0.023 ± 1
1767	11	2001/11/02	2007/04/12	38.35229	22.24435	9.860	133 ± 0	23 ± 0	0.271 ± 1	0.089 ± 0
18445	15	2006/08/11	2007/05/27	38.33185	22.06115	7.047	293 ± 0	20 ± 0	0.282 ± 1	0.159 ± 1
2122	16	2001/12/29	2003/07/04	38.34422	22.03928	7.791	185 ± 71	17 ± 3	0.167 ± 30	0.133 ± 23
2423	49	2002/02/19	2007/04/26	38.37473	22.20617	10.475	330 ± 0	40 ± 0	1.303 ± 0	0.597 ± 0
2653	52	2002/03/29	2006/06/21	38.35514	22.15037	8.653	320 ± 18	37 ± 6	0.559 ± 21	0.143 ± 7
2877	39	2001/06/28	2006/12/02	38.35684	22.06999	8.179	304 ± 15	21 ± 11	1.039 ± 18	0.290 ± 12
3061	15	2002/08/05	2007/02/22	38.37292	22.03228	8.057	293 ± 26	20 ± 12	0.603 ± 30	0.143 ± 11
3147	27	2002/08/31	2007/07/24	38.35804	22.02894	8.393	266 ± 53	24 ± 10	1.179 ± 98	0.568 ± 21
3715	27	2002/06/30	2007/06/18	38.37466	22.23408	10.003	311 ± 12	19 ± 12	0.660 ± 13	0.269 ± 8
3803	15	2001/05/20	2004/07/26	38.33893	22.05582	7.586	269 ± 70	24 ± 12	1.037 ± 86	0.159 ± 11
3911	30	2003/12/27	2004/01/23	38.29883	22.09572	7.247	282 ± 30	45 ± 11	0.286 ± 20	0.103 ± 23
3917	21	2003/12/27	2004/03/09	38.29392	22.11025	6.077	311 ± 30	27 ± 19	0.299 ± 23	0.097 ± 12
4049	21	2002/03/23	2006/08/10	38.37488	22.15533	9.562	298 ± 27	32 ± 15	0.313 ± 15	0.273 ± 18
4416	23	2004/02/24	2004/04/01	38.30766	22.08154	7.138	231 ± 78	23 ± 19	0.507 ± 74	0.140 ± 23
4432	28	2004/01/29	2005/11/19	38.30814	22.08087	7.168	282 ± 42	38 ± 13	0.856 ± 31	0.226 ± 14
4493	15	2002/11/10	2007/01/25	38.30912	22.08328	7.614	245 ± 69	36 ± 12	0.288 ± 25	0.122 ± 12
4572	25	2004/03/11	2004/06/08	38.30905	22.05852	7.382	273 ± 44	40 ± 14	0.628 ± 11	0.143 ± 12
4605	26	2002/09/26	2004/04/06	38.30521	22.10001	6.870	265 ± 48	22 ± 20	0.432 ± 17	0.164 ± 12
4652	27	2004/09/05	2007/01/12	38.31680	22.07295	7.036	261 ± 53	25 ± 20	1.026 ± 28	0.469 ± 15
4693	15	2002/06/22	2005/10/25	38.28373	22.08658	5.599	280 ± 44	34 ± 17	0.315 ± 9	0.184 ± 18
4761	17	2004/04/10	2004/06/02	38.31186	22.03977	7.201	278 ± 43	34 ± 14	0.748 ± 25	0.313 ± 15
4961	16	2002/09/09	2007/01/08	38.41550	21.96045	9.021	264 ± 76	33 ± 15	0.557 ± 70	0.199 ± 34
5257	29	2007/01/07	2007/01/16	38.37909	22.03074	6.884	222 ± 83	36 ± 9	0.950 ± 82	0.265 ± 11
5278	26	2007/01/09	2007/02/11	38.31028	22.09139	7.419	303 ± 19	34 ± 9	0.411 ± 8	0.183 ± 5
573	18	2001/06/11	2007/02/20	38.36816	22.20335	10.199	310 ± 22	36 ± 9	0.724 ± 12	0.272 ± 6
630	11	2001/04/14	2002/11/18	38.30221	22.15344	7.578	300 ± 29	35 ± 9	0.638 ± 14	0.233 ± 10
724	20	2000/06/20	2004/07/28	38.33593	22.10491	7.983	289 ± 32	30 ± 12	0.380 ± 8	0.147 ± 7
853	21	2001/10/20	2007/02/20	38.40795	22.06650	9.882	302 ± 19	31 ± 10	0.921 ± 13	0.113 ± 9
866	58	2001/06/01	2007/06/21	38.33197	22.15463	7.886	275 ± 0	17 ± 0	0.681 ± 1	0.241 ± 0
891	13	2001/08/03	2007/04/04	38.30182	22.14909	7.013	247 ± 56	16 ± 3	0.778 ± 32	0.156 ± 12
903	28	2001/08/05	2007/05/18	38.38026	22.01601	8.198	231 ± 52	10 ± 8	1.589 ± 35	0.489 ± 17

APPENDIX B: RELATIVE ERRORS

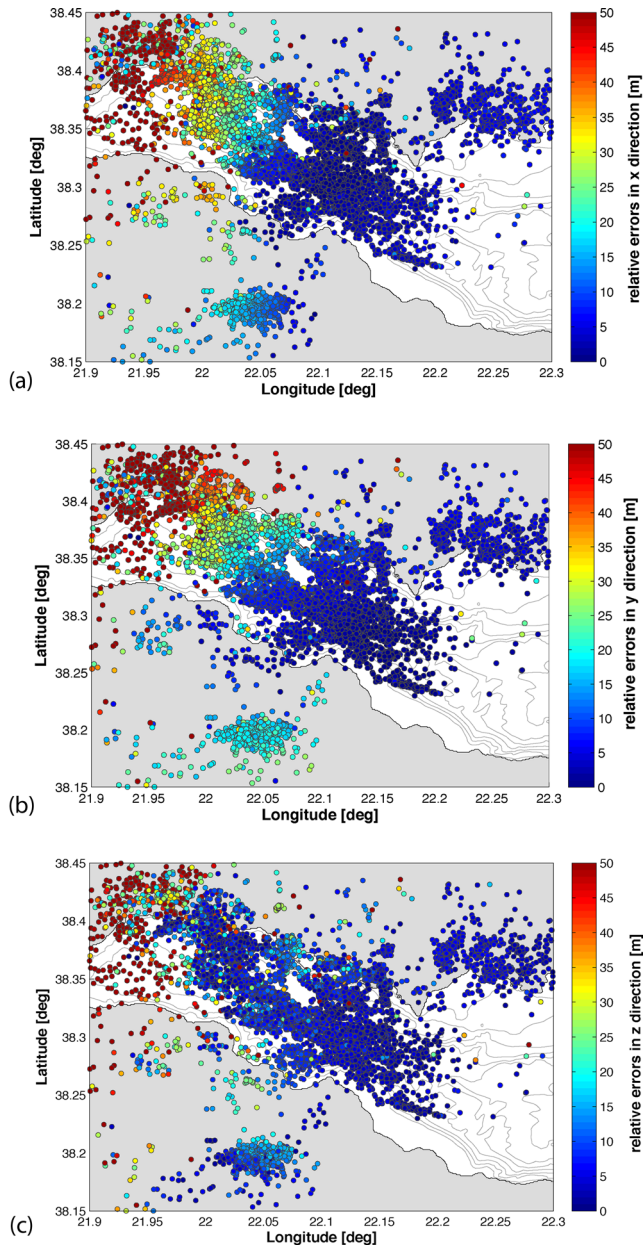


Figure B1. Map representing the relative relocation errors taking into account errors due to neighbouring events, station coverage and uncertainties on the traveltimes differences. The errors were computed applying a statistical resampling method using bootstrap technique. Errors are represented: (a) in the x -direction, (b) in the y -direction and (c) in depth. Errors are indicated in metres. Each coloured circle corresponds to a relocated events. The relative errors are smaller in the centre of the rift where the density of events and the quantity of cross-correlation data is high, and larger to the west where the network coverage is not good.

APPENDIX C: INITIAL LOCATIONS

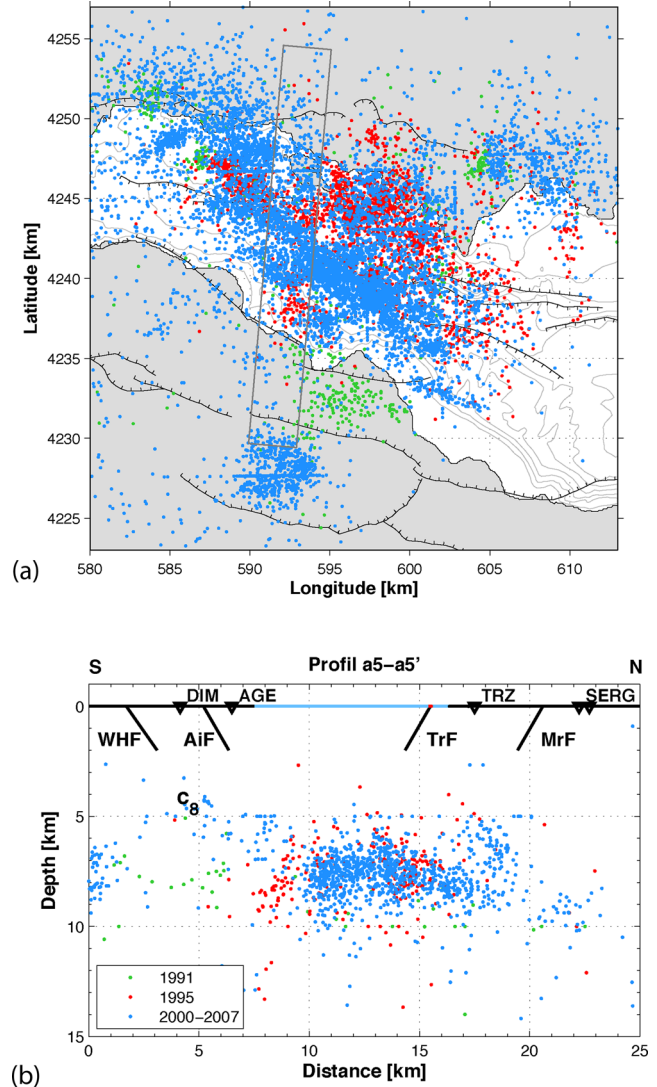


Figure C1. (a) Map of the initial location of seismicity (blue: 2000–2007, red: 1995 and green: 1991). Initial location were computed using hypo71 (Lee & Lahr 1972), with the 1-D model of Rigo *et al.* (1996), and a V_p/V_s ratio of 1.80. Main faults are indicated in black. (b) Detail of the cross-section a_5 indicated by a black rectangular box on the map. Black bold lines indicate either the major onshore and offshore faults. Light blue lines represent the offshore part of the rift. The seismicity is diffused.